



Cite this: *Nanoscale*, 2025, **17**, 6287

## Insight into the structural reconstruction of alkaline water oxidation electrocatalysts

Kaixi Wang,<sup>a,b</sup> Yifei Xu,<sup>a</sup> Vahid Daneshvariesfahlan,<sup>b</sup> Moniba Rafique,<sup>c</sup> Qiang Fu,<sup>id</sup> \*<sup>d</sup>  
 Hang Wei,<sup>id</sup> <sup>e</sup> Yumin Zhang,<sup>id</sup> <sup>a</sup> Jiheng Zhang,<sup>b</sup> Bing Zhang<sup>b</sup> and  
 Bo Song<sup>id</sup> \*<sup>a,b,c,d,f</sup>

The oxygen-evolution reaction (OER) is an indispensable component of various energy storage and conversion electrocatalytic systems. However, the slow reaction kinetics have forced the development of advanced, efficient, and inexpensive OER electrocatalysts to break through the bottleneck of its application. Recently, the structural reconstruction of precatalysts has provided a promising avenue to boost the catalytic activity of electrocatalysts. Structural reconstruction implies atomic rearrangement and composition change of the pristine catalytic materials, which is a very complex process. Therefore, it is very crucial to have a deep understanding of the reconstruction chemical process and then modulate the reconstruction by deliberate design of electrochemical conditions and precatalysts. However, a systematic review of the structural reconstruction process, research methods, influencing factors and structure–performance relationship remains elusive, significantly impeding the further developments of efficient electrocatalysts based on structural reconstruction chemistry. This critical review is dedicated to providing a deep insight into the structural reconstruction during alkaline water oxidation, comprehensively summarizing the basic research methods to understand the structural evolution process and various factors affecting the structural reconstruction process, and providing a reference and basis for regulating the dynamic reconstruction. Moreover, the impact of reconstruction on the structure and performance is also covered. Finally, challenges and perspectives for the future study on structural reconstruction are discussed. This review will offer future guidelines for the rational development of state-of-the-art OER electrocatalysts.

Received 24th December 2024,  
 Accepted 4th February 2025

DOI: 10.1039/d4nr05426a

rsc.li/nanoscale

## 1 Introduction

Global energy consumption remains highly dependent on fossil fuels, which has significant environmental and climate change implications.<sup>1–6</sup> According to the Statistical Review of World Energy 2024, fossil fuels accounted for 81% of the global energy mix in 2023, with petroleum representing 32%

of global energy consumption, followed by coal (26%) and natural gas (23%).<sup>7</sup> The World Energy Transitions Outlook 2023 points out that the global energy transition is the key to addressing the global energy and climate crisis.<sup>8</sup> High fossil fuel prices, energy security concerns and the pressing issues posed by climate change underscore the urgent need to accelerate the development of clean energy systems. Renewable energy sources such as solar energy, wind energy and hydroelectric energy have received widespread attention due to their cleanliness and sustainability as well as their wide distribution and abundance of resources.<sup>3</sup> Renewable energy coupled with electrocatalytic systems for energy storage and conversion is an attractive solution to energy and environmental challenges.<sup>9</sup> It can not only compensate for the instability of renewable energy sources and achieve efficient energy utilization, but also reduce dependence on fossil fuels while lowering carbon emissions in the chemical production processes.<sup>10,11</sup>

Over the past decade, many advanced electrocatalytic systems have been developed for efficient energy storage and conversion, including producing high-purity green hydrogen through water electrolysis,<sup>12–14</sup> obtaining high-value chemicals

<sup>a</sup>School of Astronautics, Harbin Institute of Technology, Harbin, 150001, China

<sup>b</sup>Zhengzhou Research Institute, Harbin Institute of Technology, Zhengzhou 450046, China

<sup>c</sup>National Key Laboratory of Science and Technology on Advanced Composites in Special Environments, Harbin Institute of Technology, Harbin, 150001, China.  
 E-mail: songbo@hit.edu.cn; Tel: +86-451-86403753; <https://homepage.hit.edu.cn/pages/songbo>

<sup>d</sup>School of Physics, Harbin Institute of Technology, Harbin, 150001, China

<sup>e</sup>College of Chemistry and Chemical Engineering, Inner Mongolia Engineering and Technology Research Center for Catalytic Conversion and Utilization of Carbon Resource Molecules, Inner Mongolia University, Hohhot, 010021, China

<sup>f</sup>Laboratory for Space Environment and Physical Sciences; Frontiers Science Center for Matter Behave in Space Environment, Harbin Institute of Technology, Harbin, 150001, China

or fuels *via* the electrochemical CO<sub>2</sub> reduction reaction (CO<sub>2</sub>RR),<sup>15,16</sup> ammonia production from the nitrogen reduction reaction (NRR),<sup>17,18</sup> and rechargeable metal–air batteries.<sup>19,20</sup> These fundamental electrocatalytic reactions and devices further advance the chemical industry and the field of new energy vehicles (Fig. 1). Typically, electrocatalytic transformations usually consist of two independent half-reactions, namely the small molecule reduction reaction at the cathode and the oxygen evolution reaction (OER) at the anode.<sup>21,22</sup> Therefore, the OER is an indispensable component in these electrocatalytic systems. The OER involves a four-electron transfer, which is a more complex process, leading to slow reaction kinetics and making the anode overpotential much higher than that of the cathode.<sup>23,24</sup> Thus, developing advanced, efficient, and inexpensive OER electrocatalysts is of great theoretical and practical significance for breaking through the bottleneck of large-scale application of electrocatalytic energy storage and conversion systems.<sup>25</sup>

To date, many transition metal alloys<sup>26–29</sup> and compounds have been explored for the OER, such as oxides/hydroxides,<sup>24,30,31</sup> phosphides,<sup>32–34</sup> chalcogenides,<sup>35,36</sup> nitrides,<sup>37,38</sup> perovskites,<sup>2,39</sup> metal–organic frameworks,<sup>40,41</sup> *etc.* Numerous experimental and theoretical studies have shown that most of these materials act merely as precatalysts and that they will undergo structural reconstruction at high oxidation potentials during the OER process.<sup>42–44</sup> Structural reconstruction implies atomic rearrangement, which usually leads to specific changes in the morphology, structure, and composition of the pristine catalytic materials.<sup>2,11</sup> Previous studies have indicated that the precatalyst-derived metal oxides/(oxy)hydroxides serve as the actual active species and stable phases towards the OER.<sup>45,46</sup> It should be noted that the reconstruction of catalysts is a complex process due to the complicated reaction conditions, and the reconstructed structure is not always conducive to the improvement of catalytic performance. It depends on the structure and properties of the new active components, including corrosion resistance, binding strength with OER active intermediates, electronic configuration, conductivity, *etc.*<sup>47,48</sup> In this regard, precise control of precatalyst

reconstruction is essential for optimizing the OER performance, and it requires a deep understanding of the reconstruction chemical processes, and then regulates the reconstruction by deliberate design of electrochemical conditions and precatalysts. Although some reviews about the structural reconstruction during the OER have been reported, most of them focused on summarizing the reconstruction phenomenon, typical precatalysts, advanced characterization and the regulation strategies of reconstruction.<sup>2,36,41,44,48–54</sup> Currently, a systematic review of the structural reconstruction process, research methods, influencing factors and structure–performance relationship is unavailable.

This review aims to provide a deep insight into structural reconstruction, which is critical for developing superior OER electrocatalysts. First, basic research methods to understand the structural evolution process are introduced. Subsequently, various factors affecting the structural reconstruction process are summarized, including external reaction conditions as well as the structure and component of the precatalyst itself, which provides a reference and basis for the regulation of the reconstruction process. In addition, this review also covers the impact of reconstruction on the structure and performance. Finally, challenges and perspectives for the future study on structural reconstruction are discussed. We believe this review can provide future guidelines for the rational development of advanced OER electrocatalysts.

## 2 Research methods for the structural reconstruction process

In recent years, many methods have been developed to conduct in-depth research on the structural reconstruction of precatalysts, which can be classified into four categories: electrochemical characterization, microstructure characterization, spectroscopic analysis, and density functional theory (DFT) calculations (Fig. 2). Usually, these methods need to be

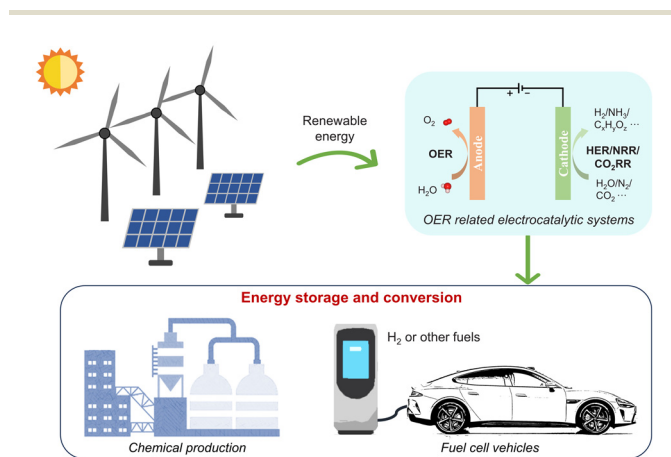


Fig. 1 Schematic of the OER-related electrochemical energy storage and conversion landscape.

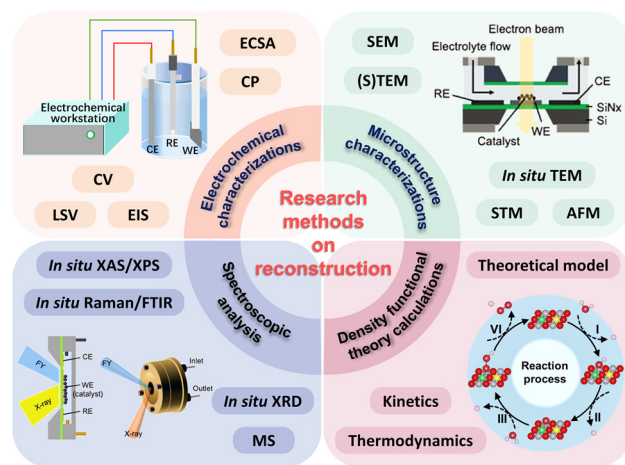


Fig. 2 Schematic illustration of various research methods for the structural reconstruction process. Reproduced with permission from ref. 55. Copyright 2020, Royal Society of Chemistry.

**Table 1** Brief summary of recent progress in the identification of reconstructed species of OER precatalysts based on various *in situ* characterization techniques

Types	Precatalysts	Electrolyte	Reconstructed (active) species	Reconstruction type	Research methods	Ref.
Oxides/hydroxides	$\beta$ -Ni(OH) <sub>2</sub>	1 M KOH	$\beta$ -NiOOH/Ni <sub>1-x</sub> O	Surface reconstruction	<i>In situ</i> TEM, Raman	57
	NiMoFeO@NC	1 M KOH	NiFeOOH/NiFe-LDH	Deep reconstruction	<i>In situ</i> Raman	62
	Mn <sub>2</sub> O <sub>3</sub>	1 M KOH	MnO <sub>x</sub>	Surface reconstruction	<i>In situ</i> TEM	68
	$\beta$ -Co(OH) <sub>2</sub>	0.1 M KOH	CoOOH	Surface reconstruction	<i>Operando</i> EC-AFM, STXM	69
	Co <sub>3</sub> O <sub>4</sub>	0.1 M KP <sub>i</sub>	CoO <sub>x</sub> (OH) <sub>y</sub>	Surface reconstruction	<i>In situ</i> grazing-incident XRD and XAS	86
Chalcogenides	V <sub>o</sub> -Co <sub>3</sub> O <sub>4</sub>	1 M KOH	Co-OOH' species	Surface reconstruction	<i>Operando</i> EIS, XAS, and <i>quasi-operando</i> XPS	67
	NiCeO <sub>x</sub> H <sub>y</sub>	1 M KOH	$\gamma$ -NiOOH	Complete reconstruction	<i>In situ</i> Raman, XRD	87
	Co <sub>3</sub> O <sub>4</sub> /Co(OH) <sub>2</sub>	1 M KOH	CoO(OH)	Surface reconstruction	<i>Operando</i> APXPS	90
	NiFeO <sub>x</sub> H <sub>y</sub>	0.1 M KOH	Fe-NiO <sub>x</sub> H <sub>y</sub>	Surface reconstruction	<i>In situ</i> ICP-MS, XAS	102
	CoS <sub>x</sub>	1 M KOH	CoOOH	Complete reconstruction	<i>In situ</i> TEM, FTIR	65
Phosphides	Co <sub>9</sub> S <sub>8</sub> @Fe <sub>3</sub> O <sub>4</sub>	1 M KOH	CoOOH@Fe <sub>3</sub> O <sub>4</sub>	Surface reconstruction	<i>In situ</i> Raman, FTIR, XAS	92
	V <sub>25%</sub> -Ni <sub>2</sub> P/NF-AC	1 M KOH	$\beta$ -NiOOH	Surface reconstruction	<i>Operando</i> EIS	66
Carbide	F-Fe-CoP	1 M KOH	F-Fe-CoOOH	Complete reconstruction	<i>In situ</i> Raman	144
	Co <sub>3</sub> C	1 M NaOH	CoO <sub>x</sub>	Complete reconstruction	—	118
Nitrides	NiMoN@NiFeN	1 M KOH + seawater	NiFe oxides/(oxy) hydroxides, Ni(OH) <sub>2</sub>	Surface reconstruction	<i>In situ</i> Raman	58
	Co <sub>3-x</sub> Fe <sub>x</sub> Mo <sub>3</sub> N	1 M KOH	CoFeMoOOH	Surface reconstruction	—	59
Borides	Ni <sub>x</sub> B	1 M KOH	Nickel oxyhydroxide	Surface reconstruction	<i>Operando</i> XAS	60
	Ir/CoNiB	1 M KOH	IrO <sub>x</sub> -oxides/(oxy) hydroxides	Surface reconstruction	<i>In situ</i> Raman, XAS, DEMS	61
MOFs	ZIF-67	1 M KOH	CoOOH/Co(OH) <sub>2</sub>	Complete reconstruction	<i>In situ</i> UV-vis, Raman	114
	CoFe <sub>2</sub> O <sub>4</sub> @CoBDC	1 M KOH	CoO <sub>x</sub> H <sub>y</sub>	Complete reconstruction	<i>In situ</i> Raman	76
Alloys	FeNi <sub>3</sub> and NiCu	1 M KOH	Fe doped NiOOH and Cu doped NiOOH	Complete reconstruction	<i>Operando</i> ATR FT-IR	93
	CrMnFeCoNi	0.05 M KOH	NiFe-rich oxyhydroxide/Mn-rich oxide	Surface reconstruction	SFC-ICP-MS	101
Others	Sr <sub>2</sub> CoO <sub>3-x</sub> F	1 M KOH	CoOOH <sub>x</sub>	Deep reconstruction	<i>In situ</i> Raman, XAS, DEMS	77
	Co <sub>2</sub> (OH) <sub>3</sub> Cl@NiMoO <sub>4</sub>	1 M KOH	CoOOH@NiOOH	Complete reconstruction	<i>In situ</i> Raman, FTIR	91

used in combination to reveal structural reconstruction behavior and reaction mechanisms (Table 1).

### 2.1 Electrochemical characterization

Electrochemical characterization techniques such as cyclic voltammetry (CV), linear sweep voltammetry (LSV), electrochemically active surface area (ECSA), chronopotentiometry (CP), *operando* electrochemical impedance spectroscopy (EIS), *etc.* are simple and effective means to identify whether catalysts undergo structural reconstruction or not, because electrochemical signals are very sensitive to changes in the structure of the electrode material, and even small structural changes will be reflected in electrochemical curves.<sup>56</sup> For example, Zhu's group reported that the current density of the  $\beta$ -Ni(OH)<sub>2</sub> precatalyst could be continuously enhanced with increasing CV scan cycles. After 1000 cycles, the current density reached a remarkable value of  $\sim 60$  mA cm<sup>-2</sup> at 1.5 V, which is more than 16 times the pristine activity (Fig. 3a), suggesting the structural reconstruction of  $\beta$ -Ni(OH)<sub>2</sub> in this process.<sup>57</sup> The shift of the

Ni redox potential towards lower values implies that the behavior of the active Ni species is responsible for the activity enhancement. In addition, the double-layer capacitance (*C*<sub>dl</sub>) and ECSA were measured to evaluate the variation of surface active sites. As shown in Fig. 3b, both *C*<sub>dl</sub> and ECSA show an obvious rise with further CV cycling, indicating the generation of more exposed active sites during the OER. Moreover, the LSV curves can provide evidence about the structural reconstruction phenomenon.<sup>62,63</sup> Wang *et al.* found that the performance of NiMoFeO@NC was significantly enhanced after continuous LSV scanning due to the self-reconstruction process.<sup>62</sup>

Another differentiation criterion is the stability test at a constant potential for a long time using the CP technique.<sup>64,65</sup> Taking the CoS<sub>x</sub> precatalyst as an example, Fan *et al.* confirmed the transformation process of Co species from CoS<sub>x</sub> to Co(OH)<sub>2</sub> and then to CoOOH through analyzing the chronopotentiometry curve of CoS<sub>x</sub> at an anodic current density of 0.5 mA cm<sup>-2</sup>.<sup>65</sup> As shown in Fig. 3d, the CP curve can be

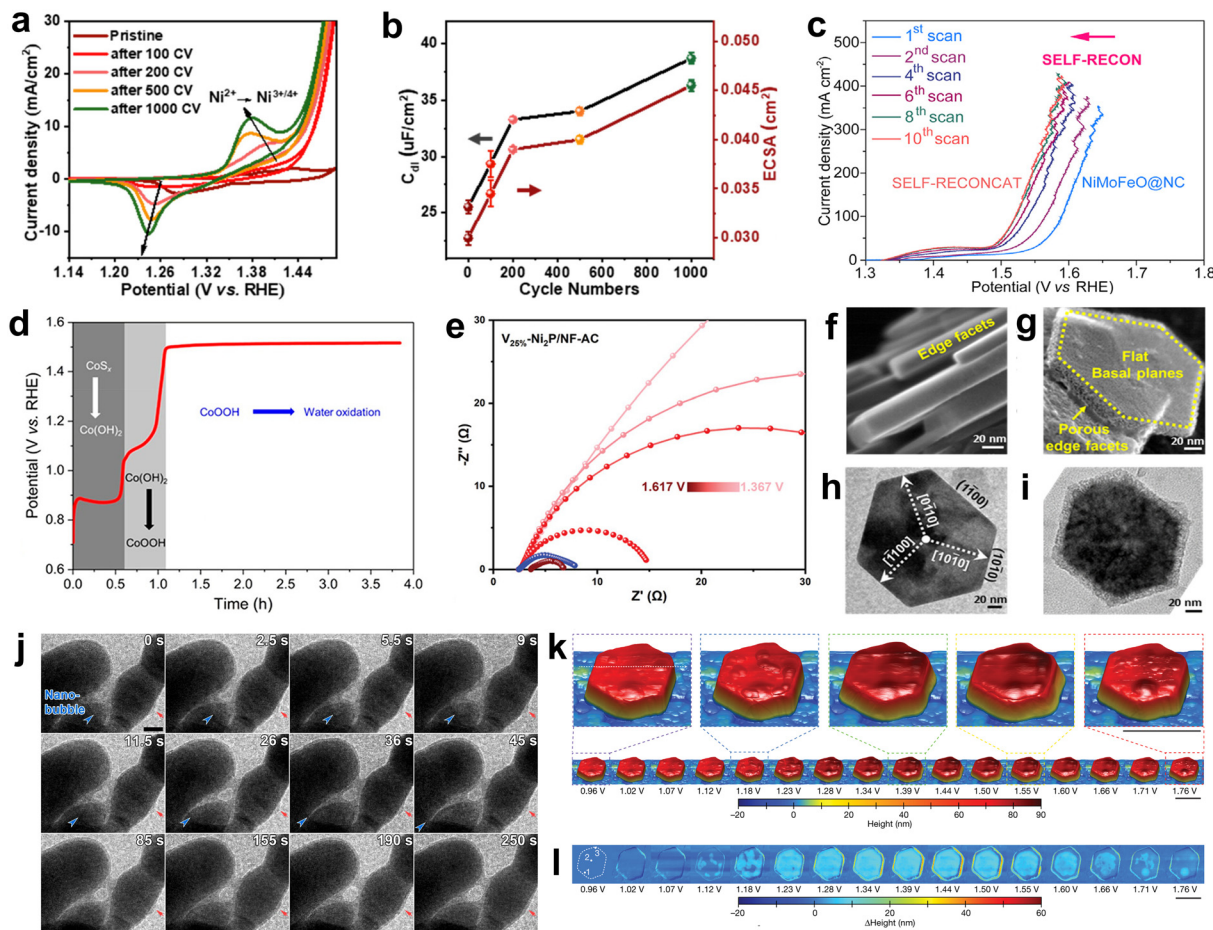


**Fig. 3** (a) CV curves at a scan rate of  $5 \text{ mV s}^{-1}$  after 80% *iR*-correction in 1 M KOH. (b)  $C_{dl}$  and ECSA values after different numbers of CV cycles under an OER potential window of 1.1–1.6 V. Reproduced with permission from ref. 57. Copyright 2024, American Chemical Society. (c) LSV curves of OER catalysis on NiMoFeO@NC after different LSV scans in 1 M KOH. Reproduced with permission from ref. 62. Copyright 2020, Elsevier. (d) Chronopotentiometry curve of  $\text{CoS}_x$  at a low anodic current density of  $0.5 \text{ mA cm}^{-2}$ . Reproduced with permission from ref. 65. Copyright 2018, American Chemical Society. (e) Operando EIS measurement of  $\text{V}_{25\%}\text{-Ni}_2\text{P/NF-AC}$  at different applied potentials *versus* RHE in 1 M KOH. Reproduced with permission from ref. 66. Copyright 2021, Wiley-VCH. (f and g) BSE-STEM images of  $\beta\text{-Ni(OH)}_2$  before and after structural reconstruction. (h and i) TEM images of  $\beta\text{-Ni(OH)}_2$  before and after structural reconstruction. Reproduced with permission from ref. 57. Copyright 2024, American Chemical Society. (j) *In situ* TEM sequential images showing the evolution of both surface layer and oxygen nanobubble associated with the OER on the  $\text{Mn}_2\text{O}_3$  nanocatalyst surface. Reproduced with permission from ref. 68. Copyright 2021, American Chemical Society. (k) Operando EC-AFM images of a  $\beta\text{-Co(OH)}_2$  particle in 0.1 M KOH at different applied voltages. Scale bars, 500 nm. (l) Differential height compared to the particle morphology at the open-circuit voltage (0.96 V). Scale bar: 500 nm. Reproduced with permission from ref. 69. Copyright 2021, Springer Nature.

divided into three parts: the electrochemical transformation of  $\text{CoS}_x$  into the  $\text{Co(OH)}_2$  intermediate takes place in the first part ( $\sim 0\text{--}0.6 \text{ h}$ ). This is followed by the second part ( $\sim 0.6\text{--}1.1 \text{ h}$ ), where  $\text{Co(OH)}_2$  experiences ion intercalation and converts to the  $\text{CoOOH}$  phase prior to reaching OER conditions. Finally, the derived  $\text{CoOOH}$  serves as the true catalytic species for a stable OER in the third part (above  $\sim 1.1 \text{ h}$ ). Besides, EIS is also used to track the structural reconstruction process, as reconstructed structures typically exhibit different electron transfer rates.<sup>66,67</sup> For instance, Zhao *et al.* conducted operando EIS measurements of  $\text{V}_{25\%}\text{-Ni}_2\text{P/NF-AC}$  to study the optimized adsorption of  $\text{*OH}$  reaction intermediates during the OER (Fig. 3e).<sup>66</sup> The smaller charge transfer resistance ( $R_{ct}$ ) with increasing applied potential suggests the evolution of  $\text{*OH}$  intermediates on the catalyst surface.

## 2.2 Microstructure characterization

Electrochemical characterization can be viewed as an indirect means of determining the structural reconstruction of precatalysts, whereas microstructure characterization allows the observation of the reconstructed samples, providing direct research tools for structural reconstruction. Many classic characterization techniques, such as scanning electron microscopy (SEM), transmission electron microscopy (TEM), scanning transmission electron microscopy (STEM), atomic force microscopy (AFM) and scanning tunneling microscopy (STM) have been employed to detect the morphological and structural transformation of precatalysts.<sup>50,52,70</sup> For example, back-scattered electrons scanning TEM (BSE-STEM) and *ex situ* TEM were carried out to explore the structure origin of the OER

improvement for the derived  $\beta$ -Ni(OH)<sub>2</sub>.<sup>57</sup> Fig. 3f–i unveils the formation of a nanoporous surface layer at the edge of the basal plane, which contrasts sharply with the smooth and flat edge surface of the pristine material.

*Ex situ* characterization techniques usually only provide indirect information about OER process studies, and are unable to perform real-time monitoring and capture reaction intermediates during the catalytic process, thus limiting the in-depth understanding of the reaction process. Therefore, *in situ* research methods are indispensable for an accurate survey of the reconstruction and can offer guidance for the rational design of high-performance electrocatalysts.<sup>71</sup> *In situ* TEM allows direct observation of the catalytic process and catalyst evolution.<sup>65,68,72,73</sup> Zhu's group utilized an *in situ* liquid holder in a TEM to unravel the real-time formation of a surface layer on Mn<sub>2</sub>O<sub>3</sub> and surrounding oxygen nanobubbles.<sup>68</sup> As shown in Fig. 3j, overall, the volume of the nanobubble increases with time. However, the bubble does not grow continuously but displays volume oscillation, which is due to the competition between oxygen evolution and dissolution. In this way, the volume change of O<sub>2</sub> bubbles can be used as an indicator to evaluate the OER rate. Meanwhile, it can be easily observed that nucleation occurs on the surface layer, which then extends across the entire surface of the nanoparticle. Throughout this process, the full size of the nanoparticle remains nearly unchanged, suggesting that the surface layer is formed *via* the reaction of surface Mn<sub>2</sub>O<sub>3</sub>, rather than through the deposition of an overlayer. In addition, the surface layer also exhibits oscillatory growth, indicating a partially reversible surface restructuring during the OER.

As a widely accepted non-contact surface analysis technique, AFM employs an atomically sharp tip to scan the sample surface. During this process, the tip detects subtle changes in the forces between the tip and the surface atoms, and by tracking the position changes of the tip attached to a microcantilever, it achieves atomic resolution imaging of the sample surface. This technique can detail the 3D topography of the sample surface. Mefford *et al.* used electrochemical atomic force microscopy (EC-AFM) effectively to investigate the *in situ* 3D morphology transformation of CoO<sub>x</sub>H<sub>y</sub> with voltage during the OER process.<sup>69</sup> As depicted in Fig. 3k and l, the particle morphology varies non-monotonically with voltage during oxidation. It is disclosed that the catalysts' lateral expansion reached a maximum at an intermediate potential of 1.39 V, and subsequently, the dimensions reverted to almost their original state as the applied potential was raised to 1.58 V. Finally, with a further increase in the voltage, the particle starts to shrink from the outer edges and moves towards the center of the particle.

### 2.3 Spectroscopic characterization

Spectroscopic characterization, especially *in situ* spectroscopic techniques, plays a pivotal role in the study of structural reconstruction of OER precatalysts. By monitoring the dynamic changes of catalysts under reaction conditions in real time, they reveal the real structure and evolution of active species,

thereby providing a deep understanding of the catalytic mechanisms and guiding the design of more efficient and stable OER catalysts.<sup>74</sup> Among numerous *in situ* spectroscopy techniques, *in situ* Raman<sup>75–80</sup> and X-ray absorption spectroscopy (XAS)<sup>81–85</sup> are the most commonly used. Besides, other spectroscopic analysis techniques like *in situ* XRD,<sup>86,87</sup> X-ray photoelectron spectroscopy (XPS),<sup>88–90</sup> Fourier transform infrared (FTIR) spectroscopy,<sup>91–93</sup> and mass spectrometry (MS)<sup>77,94</sup> are also explored to study the structural evolution process of OER precatalysts (Fig. 4).

**2.3.1 Raman spectroscopy.** Raman spectroscopy is a molecular vibrational spectroscopy technique based on the Raman scattering effect, which is used to study molecular vibration, rotation and other microstructure information, and applied to molecular structure analysis. Each substance has its own unique Raman fingerprints, which can be used as a basis for substance identification. Combining Raman spectroscopy with electrochemical methods can offer information on the microstructure of molecules and intermediates on the electrode surface under real reaction conditions, which provides a powerful means to study the electrochemical reaction mechanism and the surface reconstruction process of precatalysts. By monitoring the intensities and shifts of Raman peaks, researchers can detect the formation of new phases and the transformation of the catalyst surface under electrochemical conditions. Zhu's group conducted *in situ* Raman spectroscopy tests to probe the structural reconstruction and catalytic mechanism of  $\beta$ -Ni(OH)<sub>2</sub> during the OER (Fig. 5a).<sup>57</sup> It can be seen that in the absence of an applied potential, the Raman spectrum initially shows only peaks corresponding to  $\beta$ -Ni(OH)<sub>2</sub> (Fig. 5c). When the applied potential increases to 1.51 V, two distinct peaks appear at 473 and 555 cm<sup>-1</sup>, which are con-

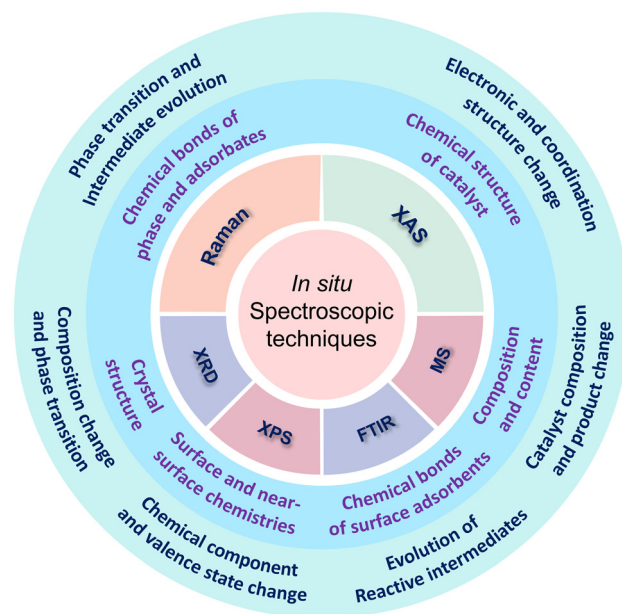
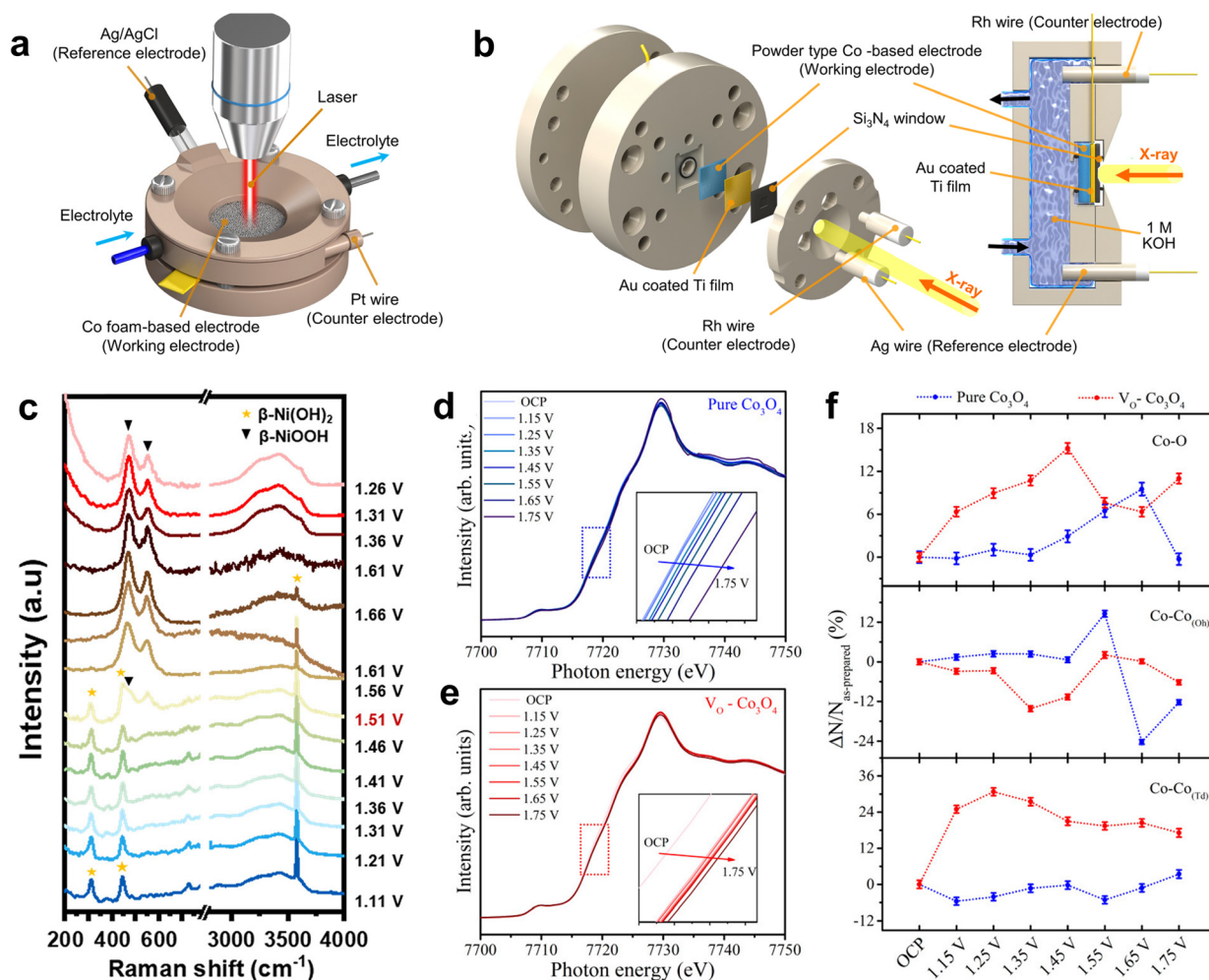


Fig. 4 Schematic illustration of the *in situ* spectroscopic techniques for OER precatalysts.



**Fig. 5** Schematic illustration of the *in situ* (a) Raman spectroscopy setting and (b) NEXAFS setup. Reproduced with permission from ref. 100. Copyright 2022, Springer Nature. (c) *In situ* Raman spectra acquired under various applied potentials during the OER on pristine  $\beta$ -Ni(OH)<sub>2</sub> after 1000 CV cycles. Reproduced with permission from ref. 57. Copyright 2024, American Chemical Society. Operando XAFS for Co K-edge of (d) pure Co<sub>3</sub>O<sub>4</sub> and (e) V<sub>O</sub>-Co<sub>3</sub>O<sub>4</sub>. The insets show a detailed view of the dotted boxes, respectively. (f) Structural coherence change in the EXAFS coordination number of Co ions under an applied potential relative to the OCP state. Reproduced with permission from ref. 67. Copyright 2020, American Chemical Society.

sistent with the characteristic peaks of  $\beta$ -NiOOH, suggesting that  $\beta$ -Ni(OH)<sub>2</sub> undergoes a phase transition at this point to  $\beta$ -NiOOH. Further increasing the applied potential results in the weakening of the  $\beta$ -Ni(OH)<sub>2</sub> signal, reflecting the continued oxidation of  $\beta$ -Ni(OH)<sub>2</sub> to  $\beta$ -NiOOH. The dominance of the  $\beta$ -NiOOH signal above the OER onset potential confirms that  $\beta$ -NiOOH is the active phase responsible for catalyzing the OER.

Apart from tracking the transformation of surface phases, the detection of oxygenated intermediates, such as \*OOH or \*O-O, provides a deeper understanding of the fundamental mechanisms in the OER. The detailed mechanistic understanding is closely related to the surface reconstruction process, as the formation of active species often accompanies structural changes on the catalyst surface. However, these intermediates typically exhibit weak Raman signals, making it difficult to collect useful information. In light of this, surface-

enhanced Raman spectroscopy (SERS), known for its heightened sensitivity and spatial resolution, has been utilized for the *in situ* characterization of OER catalysts.<sup>95–97</sup> For example, Hu *et al.* constructed bifunctional Au@Ni<sub>3</sub>FeO<sub>x</sub> core-satellite superstructures to study the interfacial OER process on the Ni<sub>3</sub>FeO<sub>x</sub> catalyst.<sup>97</sup> The Au core plays the role of a SERS enhancing substrate in this structure. The SERS data indicate that the Fe atoms serve as the active centers for the initial oxidation of OH<sup>-</sup> to O-O<sup>-</sup>. The O-O<sup>-</sup> species, adsorbed between adjacent Fe and Ni sites, undergo further oxidation due to electron transfer to Ni<sup>III</sup>, leading to the formation of the final O<sub>2</sub> product.

**2.3.2 X-ray absorption spectroscopy.** XAS is a powerful characterization technique that provides information about the structure and electronic state of a material at the atomic scale. XAS includes X-ray absorption near edge structures (XANES) and extended X-ray absorption fine structures

(EXAFS). XANES primarily reflects the electronic states and chemical environment around atoms in a sample, while EXAFS is used to study the distance and coordination number between atoms.<sup>98</sup> Therefore, *in situ* XAS can monitor the valence state and local structural changes of OER catalytic sites timely under operating conditions.

Xiao and coworkers performed *in situ* XAS to identify of the dynamic reconstruction behavior of oxygen vacancy-rich  $\text{Co}_3\text{O}_4$  ( $\text{V}_\text{O}\text{-Co}_3\text{O}_4$ ) for the OER.<sup>67</sup> The Co K-edge data were recorded from the open circuit potential (OCP) to 1.75 V vs. RHE (Fig. 5d and e). As can be seen, the edge peaks of pure  $\text{Co}_3\text{O}_4$  and  $\text{V}_\text{O}\text{-Co}_3\text{O}_4$  around 7719 eV show a similar positive shift trend with increasing applied potential, indicating the oxidation of Co. However, the oxidation rate of Co ions in  $\text{V}_\text{O}\text{-Co}_3\text{O}_4$  is faster than that in pure  $\text{Co}_3\text{O}_4$ . According to the previous literature,<sup>99</sup> it means that  $\text{V}_\text{O}$  will facilitate the adsorption of OH ions on the Co sites and subsequent deprotonation process to form reactive oxygen species ( $\text{Co}\text{-OOH}^\cdot$ ). Then, the analysis of relative changes in coordination number also reveals that  $\text{V}_\text{O}$  can promote cobalt pre-oxidation and structural reconstruction during the OER. In addition, the oxygen species involved in the OER process for the pure  $\text{Co}_3\text{O}_4$  and  $\text{V}_\text{O}\text{-Co}_3\text{O}_4$  are mostly related to the octahedral cobalt coordinated oxygen and the tetrahedral cobalt coordinated oxygen, respectively (Fig. 5f). Very recently, Shao's group reported the establishment of the relationship between oxygen-evolving performance and operational structural properties on model oxides through advanced operando characterization.<sup>77</sup> They found that the pyramidal structure is more vulnerable to  $\text{OH}^-$  attack than tetrahedral and octahedral structures due to its inherent unsaturation and asymmetry as well as its constant single-electron occupancy on the active  $\text{z}2$  orbital during reaction, which facilitates the transformation from the surface to the bulk, resulting in the formation of active, amorphous, high-valence  $\text{CoOOH}_x$  with edge-sharing structures. Operando soft XAS demonstrates that the non-uniform dehydrogenation process becomes more difficult with time ( $\text{Co}^{3+}\text{OOH} \rightarrow \text{Co}^{3+/4+}\text{OOH}_x \rightarrow \text{Co}^{4+}\text{OO}$ ) due to the increased covalency of Co–O with a higher energy barrier. Lattice oxygen participates in the formation of active  $\text{CoOOH}_x$  at the expense of stability.

**2.3.3 Other spectroscopic techniques.** Other *in situ* spectroscopic techniques have also made substantial progress after decades of efforts, enabling the monitoring of the structural evolution of precatalysts during electrochemical water oxidation. *In situ* XRD is an important technique for continuously observing catalysts' crystal structures under various reaction conditions, which can reveal the formation of new phases as well as any changes in the lattice strain or defect accompanying the reaction process. Such insights are vital for deciphering the origins of catalytic activity and unraveling the mechanisms behind catalysis. For instance, Yan *et al.* utilized *in situ* XRD to elucidate the phase evolution of  $\text{Ni}(\text{OH})_2$  and  $\text{NiCeO}_x\text{H}_y$  materials throughout the OER process.<sup>87</sup> However, challenges arise in obtaining valid signals *via in situ* XRD when the precatalyst exhibits high crystallinity, low reconstruction degree or amorphous reconstructed species.

*In situ* XPS can provide real-time information about the chemical state and electronic structure changes on and near the catalyst surface under reaction conditions. Favaro *et al.* reported the utilization of operando ambient-pressure XPS (APXPS) to study the OER mechanism and structural reconstruction on  $\text{CoO}_x$  (Fig. 6a–c).<sup>90</sup> Through spectral simulation and multiplet fitting, it has been discovered that the catalyst experiences chemical and structural changes in response to the applied anodic potential. The  $\text{Co}(\text{OH})_2$  surface layer in the biphasic catalyst facilitates structural transformation, including complete oxidative conversion to  $\text{CoO}(\text{OH})$  and partial conversion of the underlying spinel  $\text{Co}_3\text{O}_4$  to  $\text{CoO}(\text{OH})$ , making the active phase thick enough to provide high concentrations of catalytic sites. In contrast, for the monophasic catalyst, only a small portion of the surface undergoes partial conversion of  $\text{Co}_3\text{O}_4$  to  $\text{Co}(\text{OH})_2$  and only a thin layer of  $\text{CoO}(\text{OH})$  is formed at the OER potential. In addition, Xiao *et al.* used quasi-operando XPS to obtain the variation of the  $\text{Co}^{2+}/\text{Co}^{3+}$  ratio in cobalt oxide at different potentials, revealing the reconstruction process of cobalt oxide during the OER.<sup>67</sup>

In addition to the above-mentioned spectroscopic analysis techniques, FTIR is also valid for probing the changes of chemical bonds during reconstruction. Most solid electrodes are impervious to infrared light, so *in situ* FTIR tests are in most cases in reflectance mode, such as attenuated total reflectance (ATR)-FTIR (Fig. 6d).<sup>56</sup> For example, Yu's group employed *in situ* FTIR and other *ex situ* characterization techniques to observe the structural evolution of the amorphous electrocatalyst  $\text{CoS}_x$  into crystallized  $\text{CoOOH}$  in the OER directly.<sup>65</sup> Ji and coworkers deployed *in situ* synchrotron radiation-based FTIR (SR-FTIR) analysis to investigate the key active intermediates during OER.<sup>92</sup> Recently, Ma *et al.* performed *in situ* FTIR to capture the signals of  $\text{Co}=\text{O}$ ,  $\text{Co}-\text{O}$  and  $\text{Mo}=\text{O}$  bonds in the OER (Fig. 6e). The significant enhancement of the  $\text{Co}=\text{O}$  signal indicates the conversion from  $\text{Co}_2(\text{OH})_3\text{Cl}$  to  $\text{CoOOH}$  caused by  $\text{Cl}^-$  leaching. Furthermore, the enhancement of  $\text{Mo}=\text{O}$  bond strength should come from the leaching of  $\text{MoO}_4^{2-}$  derived from  $\text{NiMoO}_4$  reconstruction.<sup>91</sup>

The mass spectrometry technique can identify and quantify compounds in a sample by measuring the mass and charge of the sample molecules or atoms. By integrating mass spectrometry with an electrochemical cell, electrochemical MS enables the real-time and *in situ* monitoring of electrochemical species, including reactants, intermediates, and products in the electrocatalytic process. Luan *et al.* elucidated the structure–activity–stability relationship of  $\text{CrMnFeCoNi}$  toward the OER using an online scanning flow cell inductively coupled plasma mass spectrometer (SFC-ICP-MS), providing insights into the activation and degradation mechanism of high-entropy alloy (HEA) electrocatalysts.<sup>101</sup> Markovic's group used a method of coupling *in situ* ICP-MS with isotopic labeling, and confirmed the concomitant dissolution and redeposition of Fe on the  $\text{NiFeO}_x\text{H}_y$  electrode during the OER, which is critical for the formation of a stable electrocatalyst–electrolyte interface.<sup>102</sup> Differential electrochemical mass spectrometry (DEMS) is commonly used to detect volatile or gaseous species to study the

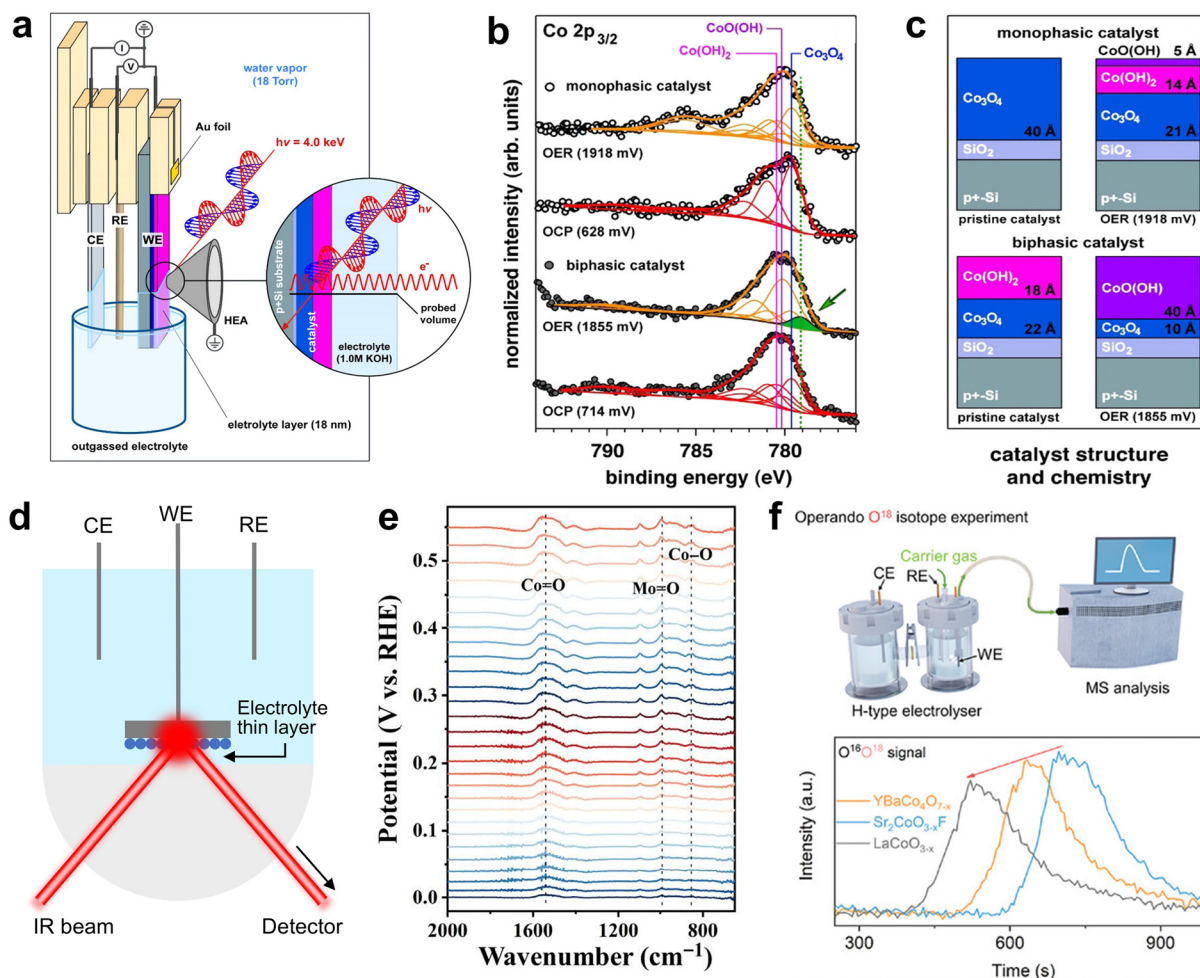


**Fig. 6** (a) Three-electrode electrochemical setup used for the operando electrochemical APXPS characterization of the OER electrocatalyst. (b) Co 2p<sub>3/2</sub> APXPS core levels acquired at the OCP and under OER conditions for two different CoO<sub>x</sub> catalysts. The green-shaded component at low BE, whose nature is explained in the text and assigned to Co<sup>4+</sup>, is observable only at OER potentials. (c) Chemical composition and subsurface structure for the monophasic and biphasic catalysts, passing from pristine to OER conditions. Reproduced with permission from ref. 90. Copyright 2017, American Chemical Society. (d) Schematic illustration of the *in situ* ATR-FTIR electrochemical cell. (e) Referred line plot of *in situ* FT-IR spectroscopy of Co<sub>2</sub>(OH)<sub>2</sub>Cl@NiMoO<sub>4</sub> in 1 M KOH during the OER. Reproduced with permission from ref. 91. Copyright 2024, Springer Nature. (f) Schematic diagram of the operando O<sup>18</sup> isotope experiment (top panel) and measured results for model oxides (bottom panel) in 1 M KOH. Reproduced with permission from ref. 77. Copyright 2024, Wiley-VCH.

OER mechanism. Shao and collaborators carried out operando O<sup>18</sup> isotope labeling experiments to directly evidence the lattice oxygen participation mechanism (LOM) on model coordinated oxides (Fig. 6f).<sup>77</sup> They labeled the partial lattice oxygen (O<sup>16</sup>) with O<sup>18</sup> isotope through electrochemical treatment, and then detected a higher intensity of the O<sup>16</sup>O<sup>18</sup> signal on pyramidal Sr<sub>2</sub>CoO<sub>3-x</sub>F, indicating its strongest LOM process in the OER.

#### 2.4 Density functional theory calculations

DFT is widely used to study the structural reconstruction of catalysts and their structure–activity relationship. Normally, the proper use of DFT should be based on a known reconstructed structure of the precatalyst. DFT calculations can optimize the geometric structure of catalysts and identify their most stable configurations, which is essential for understanding the behavior of catalysts in the OER process. DFT can help

researchers distinguish the rate-determining steps of reactions and gain an in-depth understanding of the reaction mechanism of the OER by calculating the formation energy of different intermediates and the energy changes of various reaction steps in different reaction pathways. DFT calculations can discern the active sites on the catalyst surface and analyze the effects of different elements or structures on OER performance. DFT calculations can also provide electronic structure information of catalysts, including band structure, density of states (DOS), and charge distribution. In addition, DFT calculations allow researchers to perform high-throughput screening and quickly identify catalysts with good OER performance.<sup>44,55,78,103,104</sup>

For the metal-based precatalysts, given that their dynamic structural transformation typically results in (oxy)hydroxides, which are widely regarded as the true active species in the

OER, it is essential to construct reasonable theoretical models to analyze the catalytic process. The structural models are usually determined based on the results of the *in situ* analyses described above. In addition to static DFT calculations, certain studies have implemented *ab initio* molecular dynamics (AIMD) to investigate the catalysts' dynamic behavior. For example, Zagalskaya *et al.* conducted AIMD-based simulations to examine the dissolution of Ir at the IrO<sub>2</sub>(110)/water interface.<sup>105</sup> They disclosed that IrO<sub>2</sub>OH species are produced on the surface, which are thermodynamically stable under varying electrode potentials and can be transformed into IrO<sub>3</sub> at high anodic potentials. Conversely, at low anodic potentials, Ir<sup>III</sup> is generated on the surface that can be reoxidized back to IrO<sub>2</sub>, and continue to be adsorbed as Ir<sup>III</sup>, or dissolved into the solution as Ir(OH)<sub>3</sub>. Zhou *et al.* studied the role of Fe species on NiOOH in the OER using AIMD and found that adsorption and intercalation of the Fe ion on NiOOH can introduce proton-coupled electron transfer, which significantly reduces the overpotential and promotes the OER.<sup>106</sup>

### 3. Regulating the structural reconstruction of precatalysts

Many studies have shown that the structural reconstruction of precatalysts has a significant impact on their intrinsic properties, and the reconstructed species usually exhibit enhanced OER catalytic activity compared to the pristine samples. Therefore, an in-depth understanding of the underlying reasons, the influencing factors, and their impacts on the intrinsic properties of the structural reconstruction in the OER process is crucial for elucidating the OER reaction mechanism and designing materials with controllable reconstruction, thereby promoting the development of efficient electrocatalysts. Considering the complexity of the practical electrocatalytic processes, this section will reveal and elaborate on the regulatory strategies for structural reconstruction from two critical aspects: external and intrinsic factors.

#### 3.1 External factors

The electrolyte and other electrochemical conditions (applied potential, time, and temperature) are the external triggers for inducing the structural transformation. Besides, emerging external fields (magnetic, plasma and photothermal effects) also provide efficient strategies to modulate the reconstruction behavior of precatalysts.

**3.1.1 Electrolyte.** Electrolyte is an important factor affecting catalyst reconstruction. Hausmann *et al.* found that a layered cobalt borophosphate (CoBP) precatalyst can be completely reconstructed into two kinds of cobalt oxyhydroxide (CoBP-P<sub>i</sub> and CoBP-B<sub>i</sub>) phases with different morphologies and mass transport ability depending on the electrolyte buffer.<sup>107</sup> The amorphous CoBP-P<sub>i</sub> formed in KP<sub>i</sub> shows a flat morphology with smaller domains and irreversible P<sub>i</sub> binding at the edges, leading to less available edge sites for the OER (Fig. 7a). However, the derived CoBP-B<sub>i</sub> in KB<sub>i</sub> resulted in crys-

talline nanospheres with exposed edge sites and improved proton transport (Fig. 7b), yielding an outstanding OER performance.

The pH value of the electrolyte is also known to have much influence on the reconstruction of various electrocatalysts.<sup>44,74</sup> It can directly affect the redox potential of metal species, thereby altering the electrochemical performance.<sup>108</sup> Görlin *et al.* revealed the effect of the electrolyte pH on the redox behavior and OER activity of the Ni-Fe(OOH) catalyst.<sup>109</sup> As shown in Fig. 7c, the precatalytic voltammetric charge of the redox peak couple increased significantly with increasing pH. Meanwhile, the redox peak potential showed a pH-sensitive shift towards the cathodic region, thereby enhancing OER activity by 2–3 times. In addition, for certain metal–organic frameworks (MOFs), once the pH of the electrolyte exceeds the acceptable range of these materials, it will disrupt their structure and stimulate the metal oxidation steps, thus promoting the structural reconstruction.<sup>41,110</sup> Furthermore, the pH could also affect the reconstruction degree. For example, unlike the surface reconstruction of anhydrous NiMoO<sub>4</sub> in low concentration alkaline solution (0.1–1 M KOH), high concentration industrial alkaline solution (20–30 wt% KOH) causes it to undergo complete reconstruction.<sup>111</sup>

The electrolyte additives are another factor to facilitate the structural reconstruction of precatalysts. To verify the hypothesis that the surface selenate plays a crucial role in OER performance, Shi *et al.* tested the OER activity of Ni(OH)<sub>2</sub> in 1 M KOH with the extra addition of SeO<sub>3</sub><sup>2-</sup>.<sup>112</sup> Fig. 7d shows that the OER activity improved with the addition of SeO<sub>3</sub><sup>2-</sup>, and the activity reached a maximum when the SeO<sub>3</sub><sup>2-</sup> concentration was increased to 0.1 M. Compared with Ni(OH)<sub>2</sub> in pure KOH, the current density at an overpotential of 500 mV increased from 47 to 221 mA cm<sup>-2</sup> in the presence of 0.1 M SeO<sub>3</sub><sup>2-</sup>, confirming the important contribution of surface-adsorbed chalcogenates to the OER activity. Theoretical calculations showed that the Gibbs free energy of the OER intermediates decreased after selenate adsorption, strongly substantiating the positive effect of the adsorbed selenate by promoting the adsorption of the OER intermediates. Moreover, it has been found that other additives, including SO<sub>4</sub><sup>2-</sup>, CO<sub>3</sub><sup>2-</sup>, NO<sub>3</sub><sup>-</sup>, *etc.*, can also affect the OER process. Tang *et al.* reported that the added oxyanions would be more prone to adsorb at the solid–liquid interface, which could break the dynamic balance between the adsorbed OH<sup>-</sup> ions and the release of OH<sup>-</sup> ions during the surface reconstruction process in the inner Helmholtz plane (IHP) layer. Consequently, the easier release of OH<sup>-</sup> ions into the electrolyte could expedite the surface reconstruction process (Fig. 7e). The HRTEM images show that a thicker amorphous layer of about 5 nm formed on the LaNiO<sub>3-δ</sub> surface after being immersed in electrolytes with 0.1 M SO<sub>4</sub><sup>2-</sup> (Fig. 7f), illustrating that the surface reconstruction process could be significantly promoted in the presence of oxyanions in 1 M KOH.<sup>113</sup>

**3.1.2 Other electrochemical conditions.** The applied potential is the main driving force for electrochemical reconstruction. The applied bias may exceed the redox potential of the active species, leading to possible changes in the composition

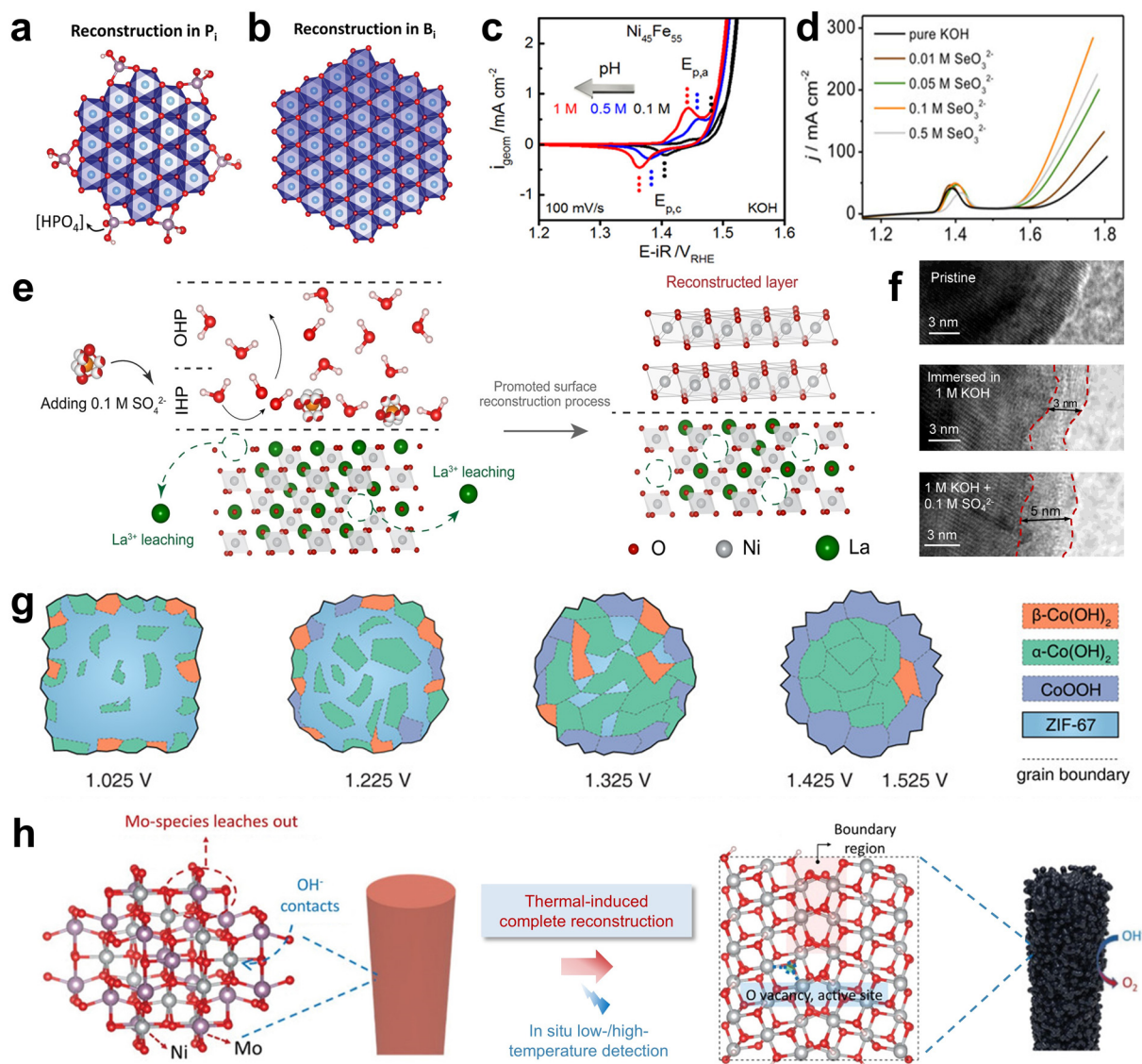


**Fig. 7** (a and b) Schemes of the reconstructed CoBP-P<sub>i</sub> and CoBP-B<sub>i</sub> in KP<sub>1</sub> and KB<sub>i</sub> electrolytes. The spheres with blue, red, purple–grey, and light-pink colors represent cobalt, oxygen, phosphorus, and hydrogen atoms, respectively. Reproduced with permission from ref. 107. Copyright 2022, Wiley-VCH. (c) CVs of the Ni<sub>45</sub>Fe<sub>55</sub> catalyst in electrolytes with different pH values. Reproduced with permission from ref. 109. Copyright 2017, American Chemical Society. (d) OER activity comparison in 1 M KOH with different SeO<sub>3</sub><sup>2-</sup> concentrations. Reproduced with permission from ref. 112. Copyright 2020, Wiley-VCH. (e) The mechanism of surface reconstruction after being immersed in electrolytes with oxyanions. (f) HRTEM images of pristine LaNiO<sub>3-δ</sub> powders, after being immersed in 1 M KOH electrolyte for 24 hours and after being immersed in 1 M KOH with the addition of 0.1 M SO<sub>4</sub><sup>2-</sup> for 24 hours. Reproduced with permission from ref. 113. Copyright 2023, Wiley-VCH. (g) Illustration of the structural evolution of ZIF-67 during amperometry at the different potential values. Reproduced with permission from ref. 114. Copyright 2019, American Chemical Society. (h) Schematic of the thermal-induced complete reconstruction on the NiMoO<sub>4</sub> nanowire. Reproduced with permission from ref. 115. Copyright 2020, Wiley-VCH.

and structure of the catalysts. Therefore, by controlling the operating potential and the applied electrochemical method, the derived catalyst can be effectively regulated. Wu *et al.* proved that the cationic defects evolve with increasing applied potential ( $V_M \rightarrow V_{MOH} \rightarrow V_{MOH-H}$ ) and revealed the essential motif of surface reconstruction in NiFe-LDH (crystalline Ni(OH)<sub>x</sub> → disordered Ni(OH)<sub>x</sub> → NiOOH).<sup>116</sup> Zheng *et al.* studied the structural and morphological evolution of ZIF-67 nanocubes during amperometry.<sup>114</sup> As shown in Fig. 7g, at

1.025 V, deformed ZIF-67 show polycrystalline structures with α and β-Co(OH)<sub>2</sub> phases on the surface and α phase in the bulk. However, as the applied potential increased to a higher potential of 1.525 V, the morphology changed from nanocubes to fractured porous spherical nanoparticles, with the surface of polycrystalline structures mainly composed of CoOOH and α-Co(OH)<sub>2</sub> in the bulk. Moreover, Xu and co-workers proposed to modulate Cr leaching in spinel CoCr<sub>2</sub>O<sub>4</sub> and surface reconstruction by activating pristine materials under high poten-

tials, which realizes the transformation of inactive  $\text{CoCr}_2\text{O}_4$  into a highly active catalyst. The scarcity of Cr and consumption of lattice oxygen promote the creation of surface defects and oxygen vacancies, which in turn allow Co species to expose and reconstruct into active Co oxyhydroxides that are distinct from  $\text{CoOOH}$ .<sup>117</sup>

Additionally, the electro-oxidation time is another key factor that affects the reconstruction process and degree. In the previous example, the authors also studied the correlation between amperometric time and OER activity.<sup>114</sup> It was found that either too long or too short a treatment time for ZIF-67 was not conducive to the optimal activity of the reconstructed catalyst, and that only a suitable duration would provide acceptable sites for optimal activity. This is because even though prolonged durations can produce sufficient sites, these sites are predominantly present in a low activity form ( $\beta\text{-Co(OH)}_2$ ), resulting in a declining turnover frequency (TOF) and reduced activity. In contrast, some studies suggest that reconstruction after sufficient treatment time is important to achieve better OER activity.<sup>118</sup> For example, Kim *et al.* reported that the amorphous  $\text{CoO}_x$  reconstructed from  $\text{Co}_3\text{C}$  after a sufficiently long oxidation time has a relatively low overpotential compared to the  $\text{Co}_3\text{C}@ \text{CoO}_x$  core-shell structure obtained in a short treatment time, which is attributed to the increased ECSA during the complete oxidation of crystalline  $\text{Co}_3\text{C}$ .<sup>118</sup> Therefore, the need for sufficient treatment time may depend on whether the reconstructed structure and composition are highly active for the OER.

Operating at relatively high temperatures has been proven to be an effective method for accelerating the reconstruction process.<sup>49</sup> High temperature can enhance mass transfer and diffusion kinetics. Mai *et al.* investigated the reconstruction process of the  $\text{NiMoO}_4$  nanowire at an industrial temperature and proposed a thermal-induced complete reconstruction strategy (Fig. 7h).<sup>115</sup> A high temperature of 51.9 °C can promote the leaching of Mo species and deep penetration of the electrolyte into the bulk. Consequently, the  $\text{NiMoO}_4$  that undergoes surface reconstruction at room temperature can achieve complete reconstruction at high temperatures. The phenomenon of high temperature deepening the reconstruction degree has also been reported by other groups.<sup>119,120</sup> For instance, Zhang *et al.* found that a higher testing temperature of  $\text{NiCo}_2\text{O}_4$  can regulate the reversible transformation of spinel-to-oxyhydroxide active species for the OER.<sup>120</sup>

**3.1.3 Emerging external fields.** The application of emerging external fields, such as magnetic, photothermal, and plasma effects, also offers effective methods to regulate the reconstruction process. Magnetic field, recognized for its non-contact and non-destructive properties, has been confirmed as a viable tool for regulating the OER performance by effects of spin polarization and spin state reconfiguration.<sup>121</sup> Xu *et al.* constructed ferromagnetic/paramagnetic (FM/PM)  $\text{Co}_{3-x}\text{Fe}_x\text{O}_4/\text{Co(Fe)O}_x\text{H}_y$  interfaces (Fig. 8a) and studied the spin pinning effect.<sup>122</sup> The spin pinning comes from a strong magnetic anisotropy field due to the strong chemical bond in the interface.<sup>123</sup> However, the magnetic domains in FM materials are

not entirely aligned in their natural state, resulting in only partial alignment of spins in  $\text{Co(Fe)O}_x\text{H}_y$  on the surface of localized magnetic domains before magnetization. After magnetization under a magnetic field, these domains can be aligned in a long-range FM order, making the spins in the PM oxyhydroxide layer become more aligned in accordance with this ordering (Fig. 8b). It should be noted that the spin pinning effect benefits from a stable oxide<sub>FM</sub>/oxyhydroxide interface and the long-range interactions are usually within 5 nm. As a result, the reconstructed  $\text{Co}_{3-x}\text{Fe}_x\text{O}_4/\text{Co(Fe)O}_x\text{H}_y$  exhibits enhanced activity after magnetization, which is different from the reconstructed sample with paramagnetic  $\text{Co}_3\text{O}_4$  as the substrate (Fig. 8c). The spin-ordered catalyst surface promotes spin polarization during the OER process and facilitates the formation of triple oxygen. Lyu *et al.* employed a magnetic field to manipulate tetrahedral units in  $\text{NiFe}_2\text{O}_4$  to boost OER performance.<sup>124</sup> It was revealed that the magnetic field can force  $\text{Ni}^{2+}$  to move from octahedral ( $\text{O}_h$ ) sites to tetrahedral (Td) sites, which show better OER catalytic activity than the  $\text{O}_h$  sites.

Studies of the effect of magnetic fields on the OER have focused on stable or reconstructed catalysts; however, the effect of magnetic fields on the reconstruction process of catalysts has rarely been investigated. Recently, our group rationally designed a ferromagnetic/paramagnetic  $\text{CoFe}_2\text{O}_4@\text{CoBDC}$  ( $\text{CFO}@\text{CoBDC}$ ) core-shell structure and systematically investigated its structural reconstruction process under magnetic fields.<sup>76</sup> It should be pointed out that a local gradient magnetic field will be induced around the ferromagnetic CFO under an external magnetic field.<sup>125</sup> Fig. 8d depicts the possible structural evolution of the Co site configuration during CV activation for  $\text{CFO}@\text{CoBDC}$ . As can be seen, the paramagnetic  $\text{Co}^{2+}$  obtained by spontaneous hydrolysis of CoBDC in alkali would be subjected to both Coulomb force ( $F_C$ ) and Kelvin force ( $F_K$ ) during activation under a magnetic field, leading to directional aggregation and stacking relatively regularly on the CFO surface. By contrast,  $\text{CFO}@\text{CoBDC}/\text{CV}$  behaves more disordered as it is only affected by  $F_C$ . Subsequently, a portion of  $\text{Co}^{2+}$  is irreversibly oxidized to  $\text{Co}^{3+}$  during the initial CV cycle. Finally, the  $\text{Co}^{2+}$  and  $\text{Co}^{3+}$  species undergo a sequence of redox reactions, forming  $\text{CoOOH}$ . In addition, even though  $\text{CoOOH}$  is the main species after activation, there is still a higher concentration of divalent Co in  $\text{CFO}@\text{CoBDC}/\text{MCV}$  under a gradient magnetic field, suggesting that  $\text{O}_v$  is to be accompanied by the generation of the  $\text{CoOOH}$  phase to balance the charge (Fig. 8e). Thus, we demonstrated that the  $F_K$  induced by a gradient magnetic field directionally modulated the surface reconstruction of CoBDC, resulting in more active  $\text{Co}^{2+}$  in derived  $\text{CoO}_x\text{H}_y$ . The Co sites with optimized electronic configuration exhibit moderate adsorption energy for oxygen-containing intermediates and lower the energy barrier of the overall catalytic reaction, thereby significantly enhancing the OER performance. This work showcases the directional structural reconstruction strategy for an improved OER.

Surface plasmon resonance (SPR) is another useful tool to regulate the reconstruction process during the OER.<sup>126,127</sup> Liu

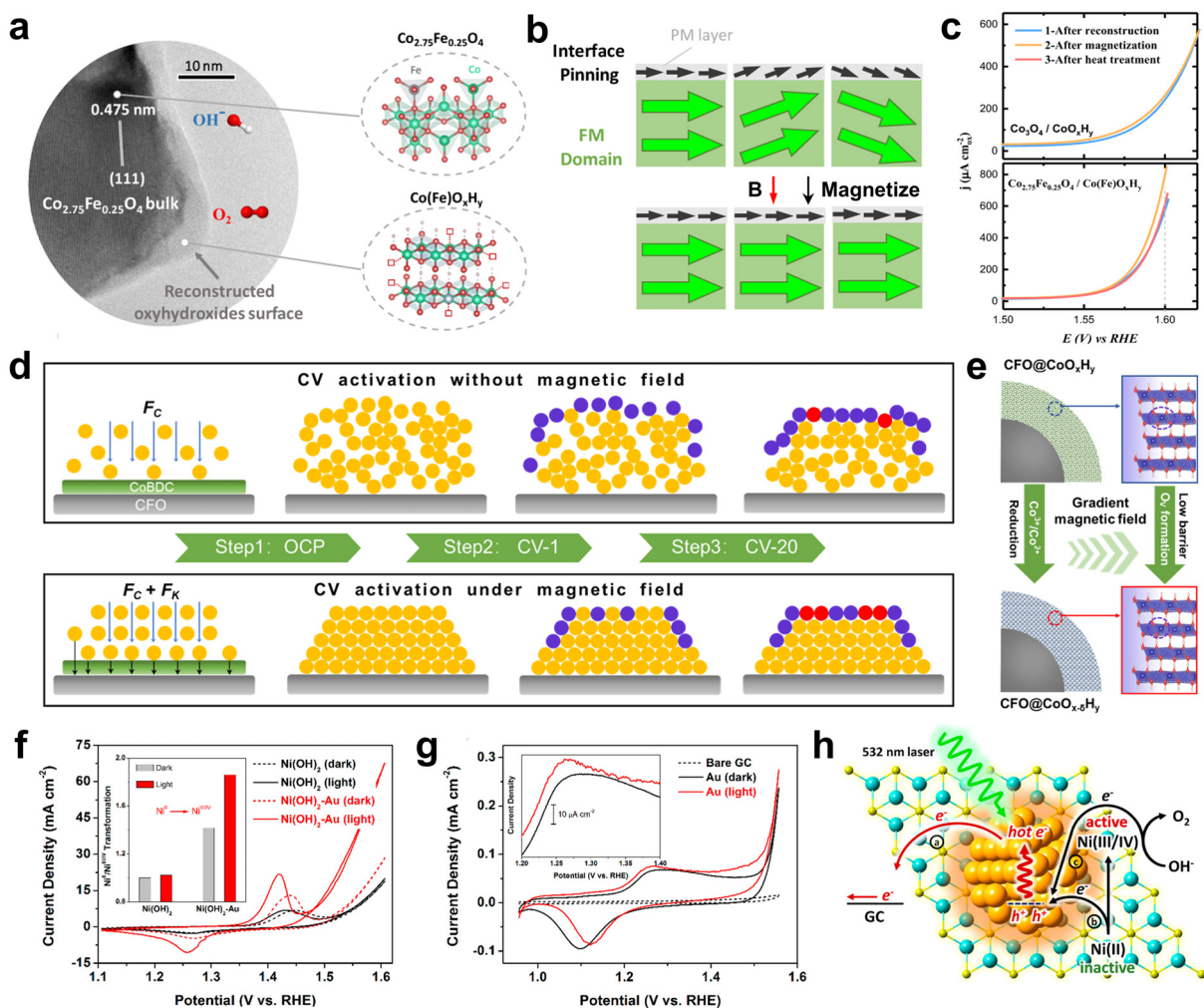


**Fig. 8** (a) The HRTEM image of  $\text{Co}_{2.75}\text{Fe}_{0.25}\text{O}_4$  after reconstruction. (b) The schematic illustration of the spin pinning effect at the interface between FM magnetic domains and the thin PM oxyhydroxide layer, and the spins in the PM oxyhydroxide layer can be aligned under magnetization. (c) LSV curves of  $\text{Co}_{3-x}\text{Fe}_x\text{O}_4$  (s) after reconstruction in 1 M KOH following different conditions. Reproduced with permission from ref. 122. Copyright 2021, Springer Nature. (d) Schematic diagram of the Co site configuration evolution model with CV activation. The yellow, blue, and red spheres represent  $\text{Co}^{2+}$ ,  $\text{Co}^{3+}$ , and Co site with  $\text{O}_v$ , respectively. (e) Schematic diagram of more  $\text{Co}^{2+}$  formation in  $\text{CFO@CoO}_x\text{H}_y$ . Reproduced with permission from ref. 76. Copyright 2024, Wiley-VCH. (f) CV curves with and without laser irradiation for  $\text{Ni}(\text{OH})_2$  nanosheets and  $\text{Ni}(\text{OH})_2\text{-Au}$  hybrids. The inset is the normalized transformation of  $\text{Ni}^{\text{II}}/\text{Ni}^{\text{III/IV}}$  on the basis of  $\text{Ni}(\text{OH})_2$  nanosheets (dark). (g) CV curves with and without laser irradiation for Au nanoparticles supported by the GC electrode. The inset displays the enlarged oxidation peaks of Au. (h) Schematic electron transfer paths in the  $\text{Ni}(\text{OH})_2\text{-Au}$  electrode under laser irradiation. The dashed line corresponds to the Fermi level of the Au nanoparticle. Yellow, cyan, and orange balls represent Ni, O, and Au atoms, respectively. Reproduced with permission from ref. 126. Copyright 2016, American Chemical Society.

*et al.* observed the plasmon-enhanced OER phenomenon on Au-nanoparticle-decorated  $\text{Ni}(\text{OH})_2$  hybrids ( $\text{Ni}(\text{OH})_2\text{-Au}$ ) after irradiation under a 532 nm laser.<sup>126</sup> The increased integrated oxidation peak area from CV curves increases with laser irradiation (Fig. 8f), which suggests that the plasmonic excitation of Au nanoparticles enhances the oxidation of  $\text{Ni}^{\text{II}}$  to  $\text{Ni}^{\text{III/IV}}$  active sites in  $\text{Ni}(\text{OH})_2\text{-Au}$ , thereby greatly improving the OER catalysis. Furthermore, the photoelectrochemical voltammetry (Fig. 8g) analysis directly indicates that SPR-excitation-induced hot-electron injection occurs on Au nanoparticles under laser irradiation. The authors put forward that during the plasmon-enhanced OER, the hot electrons produced on Au nanoparticles act as effective electron trappers to

capture electrons from  $\text{Ni}(\text{OH})_2$  and facilitate the reconstruction of inactive  $\text{Ni}^{\text{II}}$  to active  $\text{Ni}^{\text{III/IV}}$ , enabling the OER. Concurrently, the hot electrons generated by plasmon effects are transferred to the glassy carbon (GC) electrode under the external potential (Fig. 8h). The SPR-enhanced OER catalysis has also been observed with  $\text{CoO-Au}$  and  $\text{FeOOH-Au}$  catalysts, highlighting the generality of this method.

### 3.2 Intrinsic factors

In addition to the external factors mentioned above, the intrinsic causes of the precatalyst can also modulate the structural reconstruction process. Various precatalyst design strategies

with tunable morphology, composition and structure are considered as the intrinsic factors.

**3.2.1 Morphology and size control.** The structural reconstruction behavior usually begins on the surface of precatalysts, involving the participation of various substances such as electrons, intermediates, and electrolytes.<sup>128</sup> During the process, the reconstructed layer covering the surface of the precatalysts inevitably affects the rate of charge transfer and substance exchange, thus hindering further reconstruction, usually resulting in incomplete or surface reconstruction. In general, the thickness of the reconstruction layer is less than 10 nm. In this case, designing nanostructured precatalysts with at least one dimension below 10 nm can enable their complete reconstruction.<sup>49,62,129–131</sup> Ultrasmall nanoparticles, ultrathin nanosheets and ultrafine nanowires have been developed to realize the deep reconstruction. Besides, reducing catalyst size helps expose more active sites. Therefore, the OER reconstruction process can be effectively regulated by controlling the morphology and size of precatalysts.

For instance, Wu *et al.* synthesized a nickel foam (NF)-supported Ni<sub>3</sub>S<sub>2</sub> nanosheet array with a thickness of 20 nm decorated with ultrasmall Ni<sub>x</sub>Co<sub>3-x</sub>S<sub>4</sub> nanoparticles (3–5 nm in diameter) through a partial cation exchange process.<sup>132</sup> It was observed that the tiny nanoparticles completely converted into hydroxides after the OER, while the underlying crystalline structure of the nanosheets remained unchanged. In another typical example, Liu *et al.* introduced a lithiation-induced deep reconstruction strategy to obtain NiO with a size of less than 10 nm, and then these ultrasmall nanoparticles were deeply reconstructed to NiOOH through electro-oxidation.<sup>129</sup> As a comparison, only about a 5 nm-thick reconstructed NiOOH layer was generated on the surface of the bulk Ni precatalyst without lithiation, and the limited reconstruction degree is due to the impaired electrolyte permeation. Compared to the incompletely reconstructed sample, the as-fabricated completely reconstructed NiOOH achieved significantly enhanced mass activity and better stability owing to a significant increase in the number of catalytic species and the polycrystalline features with abundant defects.

**3.2.2 Component modulation-induced reconstruction.** Fine tailoring of precatalyst components provides the possibility to build highly active OER target catalysts. The electronic structure and surface physicochemical properties can be finely adjusted by introducing or substituting specific elements, leading to the activated reconstruction process and thus more electrocatalytically active species for the promoted OER.<sup>71,104</sup> The incorporation of secondary metals (Fe,<sup>133–137</sup> Ni,<sup>138</sup> Sn,<sup>139</sup> Ru,<sup>79</sup> Gd,<sup>140</sup> Sr,<sup>141</sup> *etc.*) has been found to be an effective method for optimizing reconstruction processes.

Among various metal elements, Fe is the most commonly used. In a representative work, Wu *et al.* reported an Fe substitution approach to boost the surface reconstruction and OER activity of the inactive spinel CoAl<sub>2</sub>O<sub>4</sub> (Fig. 9a).<sup>137</sup> They found that the incorporation of Fe triggers the preliminary pre-oxidation of Co at a low potential, which not only promotes surface reconstruction but also facilitates the subsequent

deprotonation process on the newly formed oxyhydroxide to induce negatively charged oxygen as an active site, thereby significantly increasing the OER activity of CoAl<sub>2</sub>O<sub>4</sub> (Fig. 9b). Further research indicated that Fe substitution elevates the O 2p band centre, which contributes to V<sub>O</sub> formation in CoFe<sub>0.25</sub>Al<sub>1.75</sub>O<sub>4</sub> with lattice oxygen oxidation. The V<sub>O</sub> accumulates on the oxide surface with great structural instability, inducing surface reconstruction into oxyhydroxides (Fig. 9c). They also investigated the reconstruction-terminating mechanism. It was revealed that the leaching of Al lowered the O 2p energy level of the oxide, leading to the termination of lattice oxygen oxidation, thus preventing further reconstruction as V<sub>O</sub> was no longer produced (Fig. 9d). Similarly, using LaNi<sub>1-x</sub>Fe<sub>x</sub>O<sub>3</sub> perovskite oxides as model catalysts, An *et al.* explored the influence of Fe substitution on the surface reconstruction process.<sup>133</sup> It was demonstrated that a low Fe content in LaNi<sub>1-x</sub>Fe<sub>x</sub>O<sub>3</sub> significantly accelerates the reconstruction rate and improves the electrocatalytic activity. Nevertheless, the reconstruction degree of LaNi<sub>1-x</sub>Fe<sub>x</sub>O<sub>3</sub> does not align with its OER activity. The volcano-shaped activity trend and the thinner reconstructed layer with increasing Fe substitution reveal that the key factor to determine the activity of reconstructed surfaces is the composition of the LaNi<sub>1-x</sub>Fe<sub>x</sub>O<sub>3</sub> perovskite, instead of the surface reconstruction degree (Fig. 9e and f). Recently, Kim and co-workers reported that the incorporation of Ru dopants into the NiFe<sub>2</sub>O<sub>4</sub>/NiMoO<sub>4</sub> heterointerface can modulate the electronic configuration and induce the high-valence state of Ni<sup>3.6+δ</sup>, which promotes the surface reconstruction to a highly active phase of Ru-doped NiFeOOH/NiOOH. DFT calculations reveal that Ru doping can enrich electron density and optimize intermediate adsorption on the active Ni species, and thus enhance the OER activity.<sup>79</sup> In addition, a strategy of electronic-ferry in metal element migration has been proposed to promote deep reconstruction of NiFe-based phosphide for the highly efficient and stable OER.<sup>142</sup>

The incorporation of nonmetallic elements to optimize the restructuring and OER kinetics of precatalysts was also widely investigated. The reported anions to date predominantly involve those with large electronegativity, such as F,<sup>143–145</sup> Cl,<sup>146–148</sup> P,<sup>149,150</sup> S,<sup>151–153</sup> and so on. For example, Zhang *et al.* introduced the F anion into the LaNi<sub>0.75</sub>Fe<sub>0.25</sub>O<sub>3</sub> (LNFO) perovskite by fluorination annealing and found that the incorporation of F can trigger a dynamic surface reconstruction to form an electrochemically active oxyhydroxide layer on the perovskite oxide, which reduces the energy barrier of the OER.<sup>143</sup> Fan *et al.* revealed that S doping can improve the reconfiguration degree of NiFe LDH nanosheets and promote the phase transformation into highly active S-doped oxyhydroxides, optimizing the adsorption of reaction intermediates and enhancing the OER kinetics.<sup>151</sup> Likewise, Su *et al.* prepared sulfur-doped NiCr LDH and studied the role of S doping in NiCr LDH for the OER.<sup>152</sup> The results indicate that S incorporation not only facilitates the reconstruction of NiCr LDH by modulating Cr leaching, but also increases the covalency of the Ni–O bond and shifts the

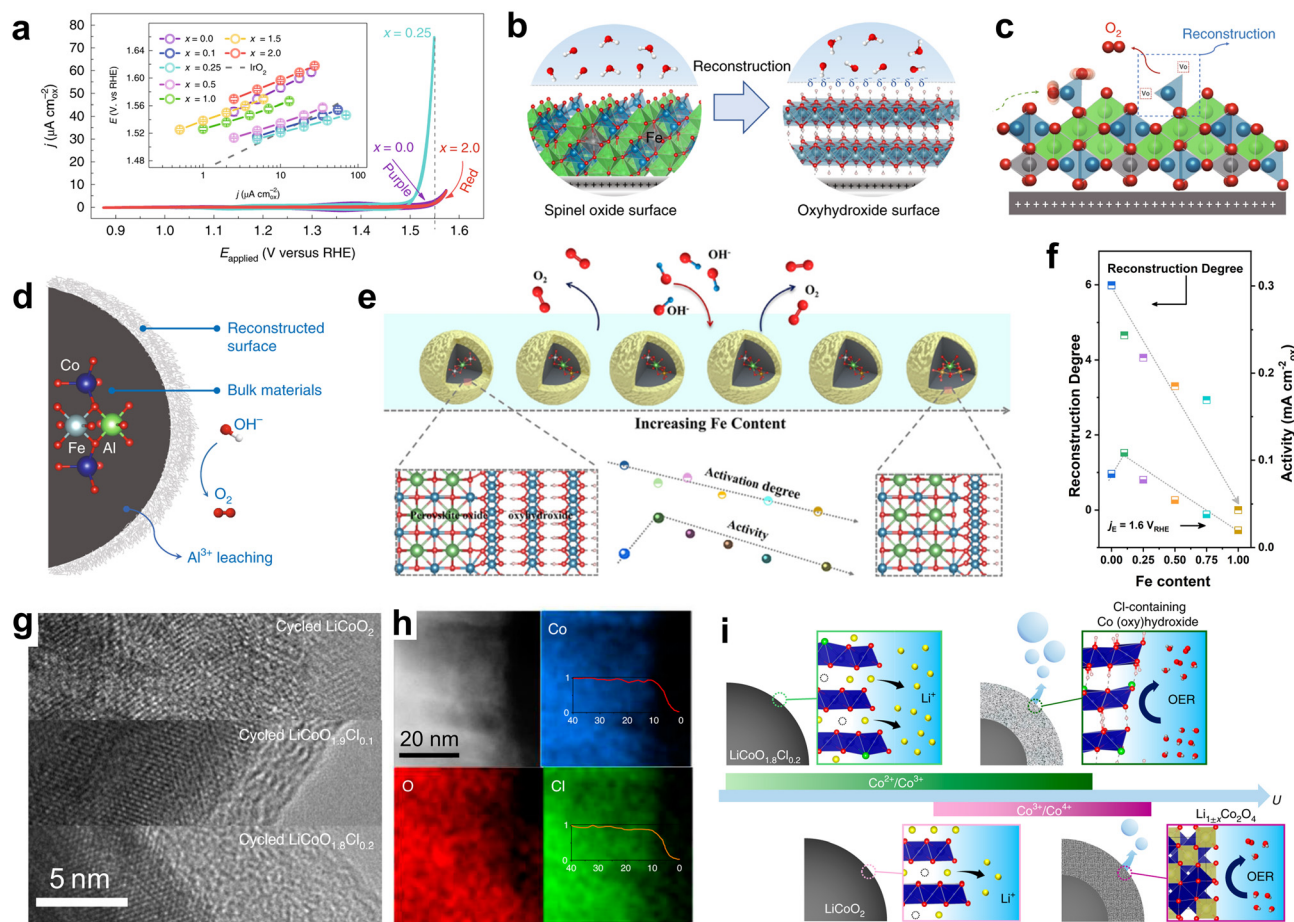


**Fig. 9** (a) CV curves of  $\text{CoFe}_x\text{Al}_{1-x}\text{O}_4$  ( $x = 0, 0.25$  and  $2$ ) in  $1\text{ M KOH}$ . The inset is the corresponding Tafel plots after oxide surface area normalization. (b) The schematic of reconstruction from spinel  $\text{CoFe}_{0.25}\text{Al}_{1.75}\text{O}_4$  into oxyhydroxide with an activated negatively charged oxygen ligand. (c) Schematic diagram of a surface reconstruction mechanism for  $\text{CoFe}_{0.25}\text{Al}_{1.75}\text{O}_4$ . Green, blue, cyan, and red balls represent Al, Co, Fe, and O atoms, respectively. (d) Schematic of  $\text{Al}^{3+}$  leaching along with surface reconstruction of the spinel oxide. Reproduced with permission from ref. 137. Copyright 2019, Springer Nature. (e) Schematic of changes in the structural reconstruction degree and OER activity with increasing Fe substitution amount. Green, blue, brown, and red balls represent La, Ni, Fe, and O atoms, respectively. (f) Current densities at  $1.6\text{ V}$  and the thickness of the newly formed reconstructed surface layer for  $\text{LaNi}_{1-x}\text{Fe}_x\text{O}_3$ . Reproduced with permission from ref. 133. Copyright 2025, Springer Nature. (g) TEM images. (h) HAADF-STEM image and the corresponding EDS mapping of the surface region. Inset is the EDS line cut. (i) Schematic diagram of the *in situ* surface restructuring process of  $\text{LiCoO}_{1.8}\text{Cl}_{0.2}$  and  $\text{LiCoO}_2$  during the OER. Yellow, blue, green, and red balls represent Li, Co, Cl, and O atoms, respectively. Reproduced with permission from ref. 147. Copyright 2021, Springer Nature.

O 2p band center to a higher position, which in turn facilitates the oxidation of lattice oxygen.

Rationally manipulating the dynamic surface reconstruction and manipulating the *in situ* formed surface active species are highly desired for an efficient OER. Wang *et al.* selected layered  $\text{LiCoO}_2$  as a model material and prepared Cl-doped  $\text{LiCoO}_2$  ( $\text{LiCoO}_{2-x}\text{Cl}_x$ ,  $x = 0, 0.1$  or  $0.2$ ) by a solid-state reaction method. They demonstrated a cationic redox-tuning approach to engineer catalyst leaching and redirect the dynamic surface restructuring of  $\text{LiCoO}_{2-x}\text{Cl}_x$  under the OER.<sup>147</sup> The TEM images display an amorphous layer on the surface of cycled  $\text{LiCoO}_{1.8}\text{Cl}_{0.2}$ , which is quite different from that of the cycled  $\text{LiCoO}_2$  (Fig. 9g). Further observation using STEM-EDS confirmed the presence of Co, O, and Cl in the reconstructed surface with no significant Cl depletion (Fig. 9h). These results together with *in situ* and *ex situ* XAS and ICP-MS analyses

revealed that Cl doping triggered the *in situ* Co oxidation and Li extraction of  $\text{LiCoO}_{1.8}\text{Cl}_{0.2}$  during the OER and the surface was transformed into self-terminated Cl-doped cobalt (oxy) hydroxide with a layered structure at a lower electrochemical potential (Fig. 9i). In contrast, Cl-free  $\text{LiCoO}_2$  required a higher potential and longer cycles to finish the surface restructuring into spinel-type  $\text{Li}_{1+x}\text{Co}_2\text{O}_4$ , leading to an inferior OER performance.

**3.2.3 Defect-induced reconstruction.** Engineering defects (anion vacancies,<sup>67,154,155</sup> cation vacancies,<sup>116,156–158</sup> ligand defects,<sup>159,160</sup> planar defects,<sup>161</sup> *etc.*) in precatalysts have also been recognized as an efficient approach to tailor the electronic structure and restructuring process toward optimized electrocatalytic OER activity. Xiao *et al.* discovered that  $\text{V}_\text{O}$  triggers the dynamic restructuring of  $\text{V}_\text{O}\text{-Co}_3\text{O}_4$ , enabling  $\text{Co}^{2+}$  oxidation at a lower potential in comparison with pristine  $\text{Co}_3\text{O}_4$ .<sup>67</sup> Gao *et al.*

reported a photothermal effect to enrich  $\text{NiFe}_2\text{O}_4$  with oxygen vacancies, which promoted the OER kinetics.<sup>155</sup> Besides, Zhang *et al.* prepared selenium vacancy-rich  $\text{CoSe}_2$  nanomeshes *via* plasma treatment on  $\text{CoSe}_2$ -diethylenetriamine layered hybrids. Selenium vacancies facilitated the formation of the catalytically active  $\text{CoOOH}$  species and led to an increased number of under-coordinated Co atoms in  $\text{CoOOH}$ , thereby endowing it with a high intrinsic activity for the OER.<sup>154</sup>

In addition to anion vacancies, cation vacancies in precatalysts also play an important role in the reconstruction processes and the related OER activities. For instance, Wu *et al.* created cationic vacancy ( $\text{Ni/Fe}$ ) defects in  $\text{NiFe-LDH}$  nanosheets through aprotic-solvent-solvation-induced leaking of metal cations. Observations from *in situ* Raman spectroscopy during the OER indicate that as the voltage increases, cation defects in  $\text{NiFe-LDH}$  promote a more facile local transformation of crystalline  $\text{Ni(OH)}_x$  into a defective state, which finally forms the local  $\text{NiOOH}$  species.<sup>116</sup> Recently, Li *et al.* have demonstrated that nickel vacancies in spinel  $\text{NiFe}_2\text{O}_4$  lead to a more pronounced level of electrochemical surface reconstruction. Additionally, DFT calculations have shown that the cation-vacancy-induced effect can facilitate surface reconstruction by enhancing the covalency of the octahedral nickel-oxygen bonds in nickel ferrite. As a result, the *in situ* formation of amorphous metal oxyhydroxides on the surface provided more active sites, which accelerated the OER kinetics.<sup>158</sup> Moreover, due to the unclear impact of structural reconstruction induced by different

vacancy defects on the OER performance, Zhang *et al.* revealed the influence mechanism of defect types on the reconstruction process and the final active structure in the OER based on oxygen-deficient and metal-deficient  $\text{Co}_3\text{O}_4$ .<sup>157</sup> It is found that cobalt oxides underwent a transformation into an amorphous  $[\text{Co(OH)}_6]$  intermediate state, and then the mismatch rates of  $^*\text{OH}$  adsorption and deprotonation resulted in irreversible catalyst reconstruction. The stronger  $^*\text{OH}$  adsorption but weaker deprotonation induced by  $\text{V}_\text{O}$  supplied the driving force for reconstruction, whereas the presence of  $\text{V}_\text{Co}$  favored dehydrogenation and reduced the reconstruction rate. Although both oxygen and cobalt vacancies triggered highly active bridge Co sites in reconstructed catalysts, cobalt vacancies led to a shortening of the Co-Co distance to 3.38 Å under compressive lattice stress, which exhibited the best OER performance.

Recently, Chen *et al.* reported the influence of planar defects such as twinning and stacking faults on the structural reconstruction and intrinsic activity of electrocatalytic materials.<sup>161</sup> They prepared an  $\text{FeCoNi/FeAl}_2\text{O}_4$  hybrid coating on commercially pure titanium *via* the double cathode sputtering deposition technique, and then induced many nanotwins and stacking faults into the coating through ultrasonic cavitation. The presence of planar defects causes the adsorption energy of metal atoms with oxygen to shift towards a more negative value, enhancing oxygenophilicity and providing conditions for rapid surface reconstruction. As a result, the synergistic effect of different types of defects introduced by ultra-

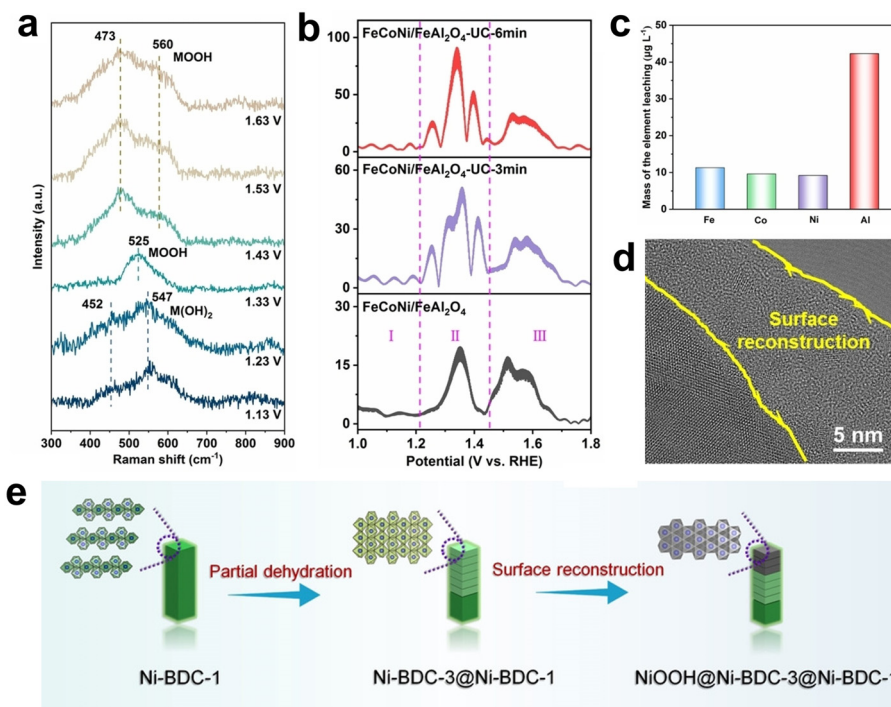


**Fig. 10** (a) *In situ* Raman spectra of  $\text{FeCoNi/FeAl}_2\text{O}_4\text{-UC-6 min}$ . (b) 5th-harmonic FTACV curves. (c) ICP-MS results for  $\text{FeCoNi/FeAl}_2\text{O}_4\text{-UC-6 min}$  after the chronopotentiometry test. (d) HRTEM image of  $\text{FeCoNi/FeAl}_2\text{O}_4\text{-UC-6 min}$ . Reproduced with permission from ref. 161. Copyright 2024, Wiley-VCH. (e) Schematic illustration of the self-reconstruction of the MOF heterojunction. Reproduced with permission from ref. 162. Copyright 2022, Wiley-VCH.

sonic cavitation activates the surface reconstruction process, allowing FeCoNi/FeAl<sub>2</sub>O<sub>4</sub>-UC-6 min to undergo surface reconstruction at an applied potential of approximately 1.33 V (Fig. 10a) and form Al-(FeCoNi)OOH species with high OER activity. The Fourier transformed alternating current voltammetry (FTACV) curves indicate that the ultrasonically cavitated coating not only possesses a higher current density, but also initiates the surface reconstruction at a lower applied voltage (Fig. 10b), which is consistent with the *in situ* Raman data. The ICP-MS result in Fig. 10c shows that the leaching amounts of Fe, Co, and Ni are nearly identical throughout the OER process, which may be due to the involvement of all three elements in the surface reconstruction process. The HRTEM image of FeCoNi/FeAl<sub>2</sub>O<sub>4</sub>-UC-6 min after the test displays low crystallinity of the metal (oxy) hydroxide layer with a thickness exceeding 10 nm (Fig. 10d). In contrast to a typical reconstruction layer thickness of a few nanometers, FeCoNi/FeAl<sub>2</sub>O<sub>4</sub>-UC-6 min with various defect types undergoes a deeper surface reconstruction, and the thicker reconstruction layer enables the stability of the catalyst.

**3.2.4 Other factors.** The carbon layer protection strategy has been used to suppress surface reconstruction. Wan *et al.* fabricated a bifunctional NiFe catalyst encapsulated within a CNT architecture through a direct pyrolysis of the carbon nitride precursor. Examination of the postcatalytic samples revealed that the presence of carbon protective shells could substantially inhibit surface restructuring, thereby reducing the creation of amorphous (oxy)hydroxide species.<sup>163</sup> Besides, the inert carbon layer can also enhance the conductivity of active components that have poor electrical conductivity, which is favorable for enhanced electrochemical activity. Yi *et al.* introduced a thermal-induced phase-segregation strategy to fabricate a SrCo<sub>0.8</sub>Fe<sub>0.5-x</sub>O<sub>3-δ</sub>/Fe<sub>x</sub>O<sub>y</sub> heterostructure catalyst for the OER.<sup>164</sup> They deduced that the segregated Fe<sub>3</sub>O<sub>4</sub> established a strong interaction with the perovskite phase, which synergistically mitigated the surface reconstruction and preserved the crystal structure's stability during the OER, thus ensuring long-term durability. In another example, Zhang *et al.* designed two analogous Ni-based MOF precatalysts (Ni-BDC-1 and Ni-BDC-3) with distinguishable topology and morphology.<sup>162</sup> Significantly, the dehydrated Ni-BDC-3, which features densely packed secondary building units, is prone to complete reconstruction into NiOOH during activation. In contrast, the hydrated Ni-BDC-1, with its weak hydrogen bonds from coordinated water molecules, resists further structural evolution, thus resulting in the formation of a stable self-reconstructed MOF heterojunction (Fig. 10e). In this structure, the MOF can serve as an electron-withdrawing agent that modulates the electronic structure of the active nickel sites of the surface-evolved NiOOH, consequently lowering the overall energy barrier for the OER loop.

## 4. Summary and outlook

Developing low-cost and efficient OER electrocatalysts is highly desirable for advanced energy storage and conversion systems.

Structural reconstruction chemistry provides a promising approach to achieve this goal. Dynamic structural reconstruction of precatalysts determines the evolution of active species and the related catalytic performance. Therefore, understanding and modulating reconstruction chemistry is pivotal for designing state-of-the-art OER electrocatalysts. In this review, we first summarized comprehensively the advanced research methods for tracking the structural reconstruction process, including electrochemical characterization, microstructure characterization, spectroscopic analysis, especially *in situ*/operando spectroscopic techniques, and DFT calculations. The combined use of these methods can provide comprehensive insights into dynamic reconstruction chemistry. Then we systematically discussed the influencing factors and regulatory strategies of precatalysts' structural reconstruction, encompassing external factors (electrolyte, other electrochemical conditions, and emerging external fields) and intrinsic factors (morphology and size of precatalysts, components, defects, *etc.*). A detailed analysis of the impact of reconstruction on the structure and performance was also carefully discussed. We hope this review will facilitate a thorough understanding of the dynamic structural reconstruction of precatalysts, and inspire the development of novel and high-performance electrocatalysts for the OER in the future.

Even though some advancements have been made in gaining insight into the structural reconstruction chemistry and designing superior electrocatalysts based on the structural reconstruction process, considerable challenges still remain: (1) The emerging external fields, such as magnetic fields, have been demonstrated to be effective methods to regulate the reconstruction process to enhance OER performance. However, the development of an external field and precatalyst types, as well as the mechanism of the effect of external fields on the reconstruction process, are still very limited, and need to be further extended and investigated. (2) Restoring the activity of degraded electrocatalysts under catalytic operating conditions is of great interest for increasing the lifetime of electrochemical devices, which can be achieved through a dynamic structural reconstruction process. There is a great need to develop new methods and recovery mechanisms to obtain ultra-long-life catalysts. (3) In most studies, the structural reconstruction occurs in low-concentration (0.1–1 M) KOH at room temperature, which is different from the industrial conditions (20–30 wt% KOH, at 50–80 °C). This will result in the unsuitability of the catalyst due to the different reconstruction processes. Hence, elucidating the fundamental mechanisms that govern structural reconstruction under practical conditions is both significant and imperative. (4) For some incompletely reconstructed precatalysts, the reconstructed species and the substrate may interact with each other, thus affecting the catalytic performance. This interaction is often overlooked but can play a crucial role in determining the overall catalytic behavior. Future research should focus on understanding and controlling these interactions to optimize the performance of electrocatalysts. (5) The tremendous progress of artificial intelligence (AI) and machine learn-

ing will undoubtedly drive the rapid development of materials science. These technologies in combination with theoretical calculations can be employed in precatalyst design and screening as well as the reconstruction process prediction to accelerate the discovery of new efficient electrocatalysts.

## Data availability

No primary research results, software or code have been included and no new data were generated or analysed as part of this review.

## Conflicts of interest

There are no conflicts to declare.

## Acknowledgements

This work was supported by the National Science Fund for Distinguished Young Scholars (grant no. 52225201), the National Natural Science Foundation of China (grant no. 52072085, 52271207, 52402242, and 52402003), the Science and Technology Development Fund, the National Key Research and Development Program of China (grant no. 2023YFE0201000), the Fundamental Research Funds for the Central Universities (grant no. HIT.BRET.2022001), the Postdoctoral Fellowship Program of CPSF (grant no. GZC20242200), the China Postdoctoral Science Foundation (grant no. 2024M764162), the Henan Province Science and Technology Research Project (grant no. 252102241037 ) and the Heilongjiang Touyan Innovation Team Program. This research is supported by the Science Foundation of the National Key Laboratory of Science and Technology on Advanced Composites in Special Environments. The authors also thank the Laboratory Center of Zhengzhou Research Institute, Harbin Institute of Technology.

## References

- 1 S. Chu and A. Majumdar, *Nature*, 2012, **488**, 294–303.
- 2 J.-W. Zhao, Y. Li, D. Luan and X. W. Lou, *Sci. Adv.*, 2024, **10**, eadq4696.
- 3 P. De Luna, C. Hahn, D. Higgins, S. A. Jaffer, T. F. Jaramillo and E. H. Sargent, *Science*, 2019, **364**, eaav3506.
- 4 K. Wang, K. N. Hui, K. S. Hui, S. Peng and Y. Xu, *Chem. Sci.*, 2021, **12**, 5737–5766.
- 5 S.-C. Sun, H. Jiang, Z.-Y. Chen, Q. Chen, M.-Y. Ma, L. Zhen, B. Song and C.-Y. Xu, *Angew. Chem., Int. Ed.*, 2022, **61**, e202202519.
- 6 H. Liu, J. Huang, K. Feng, R. Xiong, S. Ma, R. Wang, Q. Fu, M. Rafique, Z. Liu, J. Han, D. Hua, J. Li, J. Zhong, X. Wang, Z. Zhao, T. Yao, S. Jiang, P. Xu, Z. Zhang and B. Song, *Angew. Chem., Int. Ed.*, 2024, e202419595, DOI: [10.1002/anie.202419595](https://doi.org/10.1002/anie.202419595).
- 7 The Energy Institute (EI), *Statistical Review of World Energy*, 2024, <https://www.energyinst.org/statistical-review>.
- 8 International Renewable Energy Agency (IRENA), *World Energy Transitions Outlook*, 2023, <https://www.irena.org/Publications/2023/Jun/World-Energy-Transitions-Outlook-2023>.
- 9 K. Wang, S. Wang, K. S. Hui, H. Gao, D. A. Dinh, C. Yuan, C. Zha, Z. Shao, Z. Tang and K. N. Hui, *Carbon Energy*, 2022, 856–866.
- 10 J. Park, T. Kwon, J. Kim, H. Jin, H. Y. Kim, B. Kim, S. H. Joo and K. Lee, *Chem. Soc. Rev.*, 2018, **47**, 8173–8202.
- 11 F.-Y. Chen, Z.-Y. Wu, Z. Adler and H. Wang, *Joule*, 2021, **5**, 1704–1731.
- 12 K. Wang, S. Wang, K. S. Hui, J. Li, C. Zha, D. A. Dinh, Z. Shao, B. Yan, Z. Tang and K. N. Hui, *Adv. Funct. Mater.*, 2023, **33**, 2211273.
- 13 W. Zhang, M. Liu, X. Gu, Y. Shi, Z. Deng and N. Cai, *Chem. Rev.*, 2023, **123**, 7119–7192.
- 14 Q. Fu, J. C. Han, X. J. Wang, P. Xu, T. Yao, J. Zhong, W. W. Zhong, S. W. Liu, T. L. Gao, Z. H. Zhang, L. L. Xu and B. Song, *Adv. Mater.*, 2021, **33**, 1907818.
- 15 J. Du, B. Cheng, H. Yuan, Y. Tao, Y. Chen, M. Ming, Z. Han and R. Eisenberg, *Angew. Chem., Int. Ed.*, 2023, **62**, e202211804.
- 16 A. R. Woldu, Z. Huang, P. Zhao, L. Hu and D. Astruc, *Coord. Chem. Rev.*, 2022, **454**, 214340.
- 17 Y.-C. Hao, Y. Guo, L.-W. Chen, M. Shu, X.-Y. Wang, T.-A. Bu, W.-Y. Gao, N. Zhang, X. Su, X. Feng, J.-W. Zhou, B. Wang, C.-W. Hu, A.-X. Yin, R. Si, Y.-W. Zhang and C.-H. Yan, *Nat. Catal.*, 2019, **2**, 448–456.
- 18 B. H. R. Suryanto, H.-L. Du, D. Wang, J. Chen, A. N. Simonov and D. R. MacFarlane, *Nat. Catal.*, 2019, **2**, 290–296.
- 19 H.-F. Wang and Q. Xu, *Matter*, 2019, **1**, 565–595.
- 20 L. Yaqoob, T. Noor and N. Iqbal, *J. Energy Storage*, 2022, **56**, 106075.
- 21 Y. Y. Birdja, E. Pérez-Gallent, M. C. Figueiredo, A. J. Göttele, F. Calle-Vallejo and M. T. M. Koper, *Nat. Energy*, 2019, **4**, 732–745.
- 22 N. T. Suen, S. F. Hung, Q. Quan, N. Zhang, Y. J. Xu and H. M. Chen, *Chem. Soc. Rev.*, 2017, **46**, 337–365.
- 23 T. E. Jones, D. Teschner and S. Piccinin, *Chem. Rev.*, 2024, **124**, 9136–9223.
- 24 J. Huang, H. Sheng, R. D. Ross, J. Han, X. Wang, B. Song and S. Jin, *Nat. Commun.*, 2021, **12**, 3036.
- 25 Y. Zhang, Q. Fu, B. Song and P. Xu, *Acc. Mater. Res.*, 2022, **3**, 1088–1100.
- 26 X. Kang, F. Yang, Z. Zhang, H. Liu, S. Ge, S. Hu, S. Li, Y. Luo, Q. Yu, Z. Liu, Q. Wang, W. Ren, C. Sun, H.-M. Cheng and B. Liu, *Nat. Commun.*, 2023, **14**, 3607.
- 27 L. Yao, F. Zhang, S. Yang, H. Zhang, Y. Li, C. Yang, H. Yang and Q. Cheng, *Adv. Mater.*, 2024, **36**, 2314049.
- 28 M. Li, F. Lin, S. Zhang, R. Zhao, L. Tao, L. Li, J. Li, L. Zeng, M. Luo and S. Guo, *Sci. Adv.*, 2024, **10**, eadn2877.
- 29 Y.-F. Cui, S.-D. Jiang, Q. Fu, R. Wang, P. Xu, Y. Sui, X.-J. Wang, Z.-L. Ning, J. Sun, X. Sun, A. Nikiforov and B. Song, *Adv. Funct. Mater.*, 2023, **33**, 2306889.

- 30 C. Hu, X. J. Wang, T. Yao, T. L. Gao, J. C. Han, X. H. Zhang, Y. M. Zhang, P. Xu and B. Song, *Adv. Funct. Mater.*, 2019, **29**, 1902449.
- 31 W. Liu, J. Yu, T. Li, S. Li, B. Ding, X. Guo, A. Cao, Q. Sha, D. Zhou, Y. Kuang and X. Sun, *Nat. Commun.*, 2024, **15**, 4712.
- 32 X. Li, W. Xing, T. Hu, K. Luo, J. Wang and W. Tang, *Coord. Chem. Rev.*, 2022, **473**, 214811.
- 33 Q. Fu, T. Wu, G. Fu, T. L. Gao, J. C. Han, T. Yao, Y. M. Zhang, W. W. Zhong, X. J. Wang and B. Song, *ACS Energy Lett.*, 2018, **3**, 1744–1752.
- 34 B. Song, K. Li, Y. Yin, T. Wu, L. Dang, M. Cabán-Acevedo, J. C. Han, T. L. Gao, X. J. Wang, Z. H. Zhang, J. R. Schmidt, P. Xu and S. Jin, *ACS Catal.*, 2017, **7**, 8549–8557.
- 35 G. Fang, Q. Wang, J. Zhou, Y. Lei, Z. Chen, Z. Wang, A. Pan and S. Liang, *ACS Nano*, 2019, **13**, 5635–5645.
- 36 S. Zhang, Y. Cheng, P. Wang, X. Lei, J. You, R. Guo and H. Zhang, *Int. J. Hydrogen Energy*, 2024, **51**, 545–560.
- 37 X. Gao, X. Liu, W. Zang, H. Dong, Y. Pang, Z. Kou, P. Wang, Z. Pan, S. Wei, S. Mu and J. Wang, *Nano Energy*, 2020, **78**, 105355.
- 38 K. Wang, Y. Guo, Z. Chen, D. Wu, S. Zhang, B. Yang and J. Zhang, *InfoMat*, 2022, **4**, e12251.
- 39 Y. Pan, X. Xu, Y. Zhong, L. Ge, Y. Chen, J.-P. M. Veder, D. Guan, R. O'Hayre, M. Li, G. Wang, H. Wang, W. Zhou and Z. Shao, *Nat. Commun.*, 2020, **11**, 2002.
- 40 Y. Wang, B. Liu, X. Shen, H. Arandiyán, T. Zhao, Y. Li, M. Garbrecht, Z. Su, L. Han, A. Tricoli and C. Zhao, *Adv. Energy Mater.*, 2021, **11**, 2003759.
- 41 Y. Liu, S. Wang, Z. Li, H. Chu and W. Zhou, *Coord. Chem. Rev.*, 2023, **484**, 215117.
- 42 J. Feng, X. Wang and H. Pan, *Adv. Mater.*, 2024, **36**, 2411688.
- 43 S. Jin, *ACS Energy Lett.*, 2017, **2**, 1937–1938.
- 44 L. Gao, X. Cui, C. D. Sewell, J. Li and Z. Lin, *Chem. Soc. Rev.*, 2021, **50**, 8428.
- 45 D. Peng, C. Hu, X. Luo, J. Huang, Y. Ding, W. Zhou, H. Zhou, Y. Yang, T. Yu, W. Lei and C. Yuan, *Small*, 2023, **19**, e2205665.
- 46 H. Jiang, Q. He, X. Li, X. Su, Y. Zhang, S. Chen, S. Zhang, G. Zhang, J. Jiang, Y. Luo, P. M. Ajayan and L. Song, *Adv. Mater.*, 2019, **31**, 1805127.
- 47 J. Wang, *Curr. Opin. Electrochem.*, 2023, **39**, 101304.
- 48 J. Wang, *Chem*, 2023, **9**, 1645–1657.
- 49 X. Liu, J. Meng, J. Zhu, M. Huang, B. Wen, R. Guo and L. Mai, *Adv. Mater.*, 2021, **33**, 2007344.
- 50 W. Shen, J. Yin, J. Jin, Y. Hu, Y. Hou, J. Xiao, Y.-Q. Zhao and P. Xi, *Adv. Energy Sustainability Res.*, 2022, **3**, 2200036.
- 51 L. Wu, Z. Guan, D. Guo, L. Yang, X. Chen and S. Wang, *Small*, 2023, **19**, 2304007.
- 52 G. M. Tomboc, S. Venkateshalu, Q.-T. Ngo, S. Choi, B. G. Pollet, H. Lee and K. Lee, *Chem. Eng. J.*, 2023, **454**, 140254.
- 53 H. Jia, N. Yao, J. Zhu and W. Luo, *Chem. – Eur. J.*, 2023, **29**, e202203073.
- 54 N. C. S. Selvam, L. Du, B. Y. Xia, P. J. Yoo and B. You, *Adv. Funct. Mater.*, 2021, **31**, 2008190.
- 55 J. Wang, Y. Gao, H. Kong, J. Kim, S. Choi, F. Ciucci, Y. Hao, S. Yang, Z. Shao and J. Lim, *Chem. Soc. Rev.*, 2020, **49**, 9154–9196.
- 56 W. Wang, J. Duan, Y. Liu and T. Zhai, *Adv. Mater.*, 2022, **34**, 2110699.
- 57 Y. Yao, G. Zhao, X. Guo, P. Xiong, Z. Xu, L. Zhang, C. Chen, C. Xu, T.-S. Wu, Y.-L. Soo, Z. Cui, M. M.-J. Li and Y. Zhu, *J. Am. Chem. Soc.*, 2024, **146**, 15219–15229.
- 58 L. Yu, Q. Zhu, S. W. Song, B. McElhenny, D. Z. Wang, C. Z. Wu, Z. J. Qin, J. M. Bao, Y. Yu, S. Chen and Z. F. Ren, *Nat. Commun.*, 2019, **10**, 5106.
- 59 C. Zhong, J. Zhang, L. Zhang, Y. Tu, H. Song, L. Du and Z. Cui, *ACS Energy Lett.*, 2023, **8**, 1455–1462.
- 60 J. Masa, I. Sinev, H. Mistry, E. Ventosa, M. de la Mata, J. Arbiol, M. Muhler, B. R. Cuenya and W. Schuhmann, *Adv. Energy Mater.*, 2017, **7**, 1700381.
- 61 C. Wang, P. Zhai, M. Xia, Y. Wu, B. Zhang, Z. Li, L. Ran, J. Gao, X. Zhang, Z. Fan, L. Sun and J. Hou, *Angew. Chem., Int. Ed.*, 2021, **60**, 27126–27134.
- 62 Y. Wang, Y. Zhu, S. Zhao, S. She, F. Zhang, Y. Chen, T. Williams, T. Gengenbach, L. Zu, H. Mao, W. Zhou, Z. Shao, H. Wang, J. Tang, D. Zhao and C. Selomulya, *Matter*, 2020, **3**, 2124–2137.
- 63 M. Miao, R. Hou, R. Qi, Y. Yan, L. Q. Gong, K. Qi, H. Liu and B. Y. Xia, *J. Mater. Chem. A*, 2019, **7**, 18925–18931.
- 64 M. Mathankumar, S. Anantharaj, A. K. Nandakumar, S. Kundu and B. Subramanian, *J. Mater. Chem. A*, 2017, **5**, 23053–23066.
- 65 K. Fan, H. Zou, Y. Lu, H. Chen, F. Li, J. Liu, L. Sun, L. Tong, M. F. Toney, M. Sui and J. Yu, *ACS Nano*, 2018, **12**, 12369–12379.
- 66 T. Zhao, X. Shen, Y. Wang, R. K. Hocking, Y. Li, C. Rong, K. Dastafkan, Z. Su and C. Zhao, *Adv. Funct. Mater.*, 2021, **31**, 2100614.
- 67 Z. Xiao, Y.-C. Huang, C.-L. Dong, C. Xie, Z. Liu, S. Du, W. Chen, D. Yan, L. Tao, Z. Shu, G. Zhang, H. Duan, Y. Wang, Y. Zou, R. Chen and S. Wang, *J. Am. Chem. Soc.*, 2020, **142**, 12087–12095.
- 68 G. Zhao, Y. Yao, W. Lu, G. Liu, X. Guo, A. Tricoli and Ye Zhu, *Nano Lett.*, 2021, **21**, 7012–7020.
- 69 J. T. Mefford, A. R. Akbashev, M. Kang, C. L. Bentley, W. E. Gent, H. D. Deng, D. H. Alsem, Y.-S. Yu, N. J. Salmon, D. A. Shapiro, P. R. Unwin and W. C. Chueh, *Nature*, 2021, **593**, 67–73.
- 70 J. Chen, H. Chen, T. Yu, R. Li, Y. Wang, Z. Shao and S. Song, *Electrochem. Energy Rev.*, 2021, **4**, 566–600.
- 71 Y. Zhao, D. P. A. Saseendran, C. Huang, C. A. Triana, W. R. Marks, H. Chen, H. Zhao and G. R. Patzke, *Chem. Rev.*, 2023, **123**, 6257–6358.
- 72 N. Ortiz Peña, D. Ihiawakrim, M. Han, B. Lassalle-Kaiser, S. Carencio, C. Sanchez, C. Laberty-Robert, D. Portehault and O. Ersen, *ACS Nano*, 2019, **13**, 11372–11381.

- 73 B. Han, K. A. Stoerzinger, V. Tileli, A. D. Gamalski, E. A. Stach and Y. Shao-Horn, *Nat. Mater.*, 2017, **16**, 121–126.
- 74 S. Zhao, Y. Yang and Z. Tang, *Angew. Chem., Int. Ed.*, 2022, **61**, e202110186.
- 75 S. Li, Z. Li, R. Ma, C. Gao, L. Liu, L. Hu, J. Zhu, T. Sun, Y. Tang, D. Liu and J. Wang, *Angew. Chem., Int. Ed.*, 2021, **60**, 3773–3780.
- 76 S. Ma, K. Wang, M. Rafique, J. Han, Q. Fu, S. Jiang, X. Wang, T. Yao, P. Xu and B. Song, *Angew. Chem., Int. Ed.*, 2024, **63**, e202412821.
- 77 D. Guan, H. Xu, Y.-C. Huang, C. Jing, Y. Tsujimoto, X. Xu, Z. Lin, J. Tang, Z. Wang, X. Sun, L. Zhao, H. Liu, S. Liu, C.-T. Chen, C.-W. Pao, M. Ni, Z. Hu and Z. Shao, *Adv. Mater.*, 2024, 2413073, DOI: [10.1002/adma.202413073](https://doi.org/10.1002/adma.202413073).
- 78 M. Ajmal, S. Zhang, X. Guo, X. Liu, C. Shi, R. Gao, Z.-F. Huang, L. Pan, X. Zhang and J.-J. Zou, *Appl. Catal., B*, 2025, **361**, 124561.
- 79 D. Kim, S. Park, J. Choi, Y. Piao and L. Y. S. Lee, *Small*, 2024, **20**, 2304822.
- 80 S. Hou, W. Li, S. Watzele, R. M. Kluge, S. Xue, S. Yin, X. Jiang, M. Döblinger, A. Welle, B. Garlyyev, M. Koch, P. Müller-Buschbaum, C. Wöll, A. S. Bandarenka and R. A. Fischer, *Adv. Mater.*, 2021, **33**, 2103218.
- 81 S. Zhao, C. Tan, C.-T. He, P. An, F. Xie, S. Jiang, Y. Zhu, K.-H. Wu, B. Zhang, H. Li, J. Zhang, Y. Chen, S. Liu, J. Dong and Z. Tang, *Nat. Energy*, 2020, **5**, 881–890.
- 82 E. Fabbri, M. Nachttegaal, T. Binninger, X. Cheng, B.-J. Kim, J. Durst, F. Bozza, T. Graule, R. Schäublin, L. Wiles, M. Pertoso, N. Danilovic, K. E. Ayers and T. J. Schmidt, *Nat. Mater.*, 2017, **16**, 925–931.
- 83 W. Cheng, S. Xi, Z.-P. Wu, D. Luan and X. W. Lou, *Sci. Adv.*, 2021, **7**, eabk0919.
- 84 M. Wang, L. Árnadóttir, Z. J. Xu and Z. Feng, *Nano-Micro Lett.*, 2019, **11**, 47.
- 85 J. Abed, S. Ahmadi, L. Laverdure, A. Abdellah, C. P. O'Brien, K. Cole, P. Sobrinho, D. Sinton, D. Higgins, N. J. Mosey, S. J. Thorpe and E. H. Sargent, *Adv. Mater.*, 2021, **33**, 2103812.
- 86 A. Bergmann, E. Martinez-Moreno, D. Teschner, P. Chernev, M. Gliech, J. F. de Araújo, T. Reier, H. Dau and P. Strasser, *Nat. Commun.*, 2015, **6**, 8625.
- 87 Z. Yan, H. Sun, X. Chen, H. Liu, Y. Zhao, H. Li, W. Xie, F. Cheng and J. Chen, *Nat. Commun.*, 2018, **9**, 2373.
- 88 F. Scholten, I. Sinev, M. Bernal and B. R. Cuenya, *ACS Catal.*, 2019, **9**, 5496–5502.
- 89 R. M. Arán-Ais, F. Scholten, S. Kunze, R. Rizo and B. R. Cuenya, *Nat. Energy*, 2020, **5**, 317–325.
- 90 M. Favaro, J. Yang, S. Nappini, E. Magnano, F. M. Toma, E. J. Crumlin, J. Yano and I. D. Sharp, *J. Am. Chem. Soc.*, 2017, **139**, 8960–8970.
- 91 H. Ma, Y. Ding, J. Li, W. Peng and L. Mai, *Nano Res.*, 2024, **17**, 7975–7983.
- 92 Q. Ji, Y. Kong, H. Tan, H. Duan, N. Li, B. Tang, Y. Wang, S. Feng, L. Lv, C. Wang, F. Hu, W. Zhang, L. Cai and W. Yan, *ACS Catal.*, 2022, **12**, 4318–4326.
- 93 B. Wang, K. Zhao, Z. Yu, C. Sun, Z. Wang, N. Feng, L. Mai, Y. Wang and Y. Xia, *Energy Environ. Sci.*, 2020, **13**, 2200–2208.
- 94 S. Geiger, O. Kasian, M. Ledendecker, E. Pizzutilo, A. M. Mingers, W. T. Fu, O. Diaz-Morales, Z. Li, T. Oellers, L. Fruchter, A. Ludwig, K. J. J. Mayrhofer, M. T. M. Koper and S. Cherevko, *Nat. Catal.*, 2018, **1**, 508–515.
- 95 Y. Shen, X.-L. Zhang, M.-R. Qu, J. Ma, S. Zhu, Y.-L. Min, M.-R. Gao and S.-H. Yu, *Nat. Commun.*, 2024, **15**, 7861.
- 96 C. Hess, *Chem. Soc. Rev.*, 2021, **50**, 3519–3564.
- 97 C. Hu, Y. Hu, C. Fan, L. Yang, Y. Zhang, H. Li and W. Xie, *Angew. Chem., Int. Ed.*, 2021, **60**, 19774–19778.
- 98 M. Newville, *Rev. Mineral. Geochem.*, 2014, **78**, 33–74.
- 99 X. Li, H. Wang, Z. Cui, Y. Li, S. Xin, J. Zhou, Y. Long, C. Jin and J. B. Goodenough, *Sci. Adv.*, 2019, **5**, eaav6262.
- 100 W. H. Lee, M. H. Han, Y.-J. Ko, B. K. Min, K. H. Chae and H.-S. Oh, *Nat. Commun.*, 2022, **13**, 605.
- 101 C. Luan, D. Escalera-López, U. Hagemann, A. Kostka, G. Laplanche, D. Wu, S. Cherevko and T. Li, *ACS Catal.*, 2024, **14**, 12704–12716.
- 102 D. Y. Chung, P. P. Lopes, P. Farinazzo Bergamo Dias Martins, H. He, T. Kawaguchi, P. Zapol, H. You, D. Tripkovic, D. Strmcnik, Y. Zhu, S. Seifert, S. Lee, V. R. Stamenkovic and N. M. Markovic, *Nat. Energy*, 2020, **5**, 222–230.
- 103 H. Zhong, Q. Zhang, J. Yu, X. Zhang, C. Wu, Y. Ma, H. An, H. Wang, J. Zhang, X. Wang and J. Xue, *Adv. Energy Mater.*, 2023, **13**, 2301391.
- 104 H. Wang, H. Wang, Q. Hu, B. Wang, X. Lei, J. You and R. Guo, *J. Alloys Compd.*, 2025, **1010**, 177225.
- 105 A. Zagalskaya and V. Alexandrov, *J. Phys. Chem. Lett.*, 2020, **11**, 2695–2700.
- 106 Y. Zhou and N. López, *ACS Catal.*, 2020, **10**, 6254–6261.
- 107 J. N. Hausmann, S. Mebs, H. Dau, M. Driess and P. W. Menezes, *Adv. Mater.*, 2022, **34**, 2207494.
- 108 J. Li, X. Chang, H. Zhang, A. S. Malkani, M.-j. Cheng, B. Xu and Q. Lu, *Nat. Commun.*, 2021, **12**, 3264.
- 109 M. Görlin, J. Ferreira de Araújo, H. Schmies, D. Bernsmeier, S. Dresch, M. Gliech, Z. Jusys, P. Chernev, R. Kraehnert and H. Dau, *J. Am. Chem. Soc.*, 2017, **139**, 2070–2082.
- 110 L. J. Han, P. Y. Tang, Á. Reyes-Carmona, B. Rodríguez-García, M. Torrén, J. R. Morante, J. Arbiol and J. R. Galan-Mascaros, *J. Am. Chem. Soc.*, 2016, **138**, 16037–16045.
- 111 X. Liu, J. S. Meng, K. Ni, R. T. Guo, F. J. Xia, J. J. Xie, X. Li, B. Wen, P. J. Wu, M. Li, J. S. Wu, X. J. Wu, L. Q. Mai and D. Y. Zhao, *Cell Rep. Phys. Sci.*, 2020, **1**, 100241.
- 112 Y. Shi, W. Du, W. Zhou, C. Wang, S. Lu, S. Lu and B. Zhang, *Angew. Chem., Int. Ed.*, 2020, **59**, 22470–22474.
- 113 Y. Tang, C. Wu, Q. Zhang, H. Zhong, A. Zou, J. Li, Y. Ma, H. An, Z. Yu, S. Xi, J. Xue, X. Wang and J. Wu, *Angew. Chem., Int. Ed.*, 2023, **62**, e202309107.
- 114 W. Zheng, M. Liu and L. Y. S. Lee, *ACS Catal.*, 2019, **10**, 81–92.

- 115 X. Liu, R. Guo, K. Ni, F. Xia, C. Niu, B. Wen, J. Meng, P. Wu, J. Wu, X. Wu and L. Mai, *Adv. Mater.*, 2020, **32**, 2001136.
- 116 Y.-j. Wu, J. Yang, T.-x. Tu, W.-q. Li, P.-f. Zhang, Y. Zhou, J.-f. Li, J.-t. Li and S.-G. Sun, *Angew. Chem., Int. Ed.*, 2021, **60**, 26829–26836.
- 117 Y. Duan, J. Y. Lee, S. Xi, Y. Sun, J. Ge, S. J. H. Ong, Y. Chen, S. Dou, F. Meng, C. Diao, A. C. Fisher, X. Wang, G. G. Scherer, A. Grimaud and Z. J. Xu, *Angew. Chem., Int. Ed.*, 2021, **60**, 7418–7425.
- 118 J.-H. Kim, K. Kawashima, B. R. Wygant, O. Mabayoje, Y. Liu, J. H. Wang and C. B. Mullins, *ACS Appl. Energy Mater.*, 2018, **1**, 5145–5150.
- 119 P. Wilde, S. Dieckhöfer, T. Quast, W. K. Xiang, A. Bhatt, Y.-T. Chen, S. Seisel, S. Barwe, C. Andronescu, T. Li, W. Schuhmann and J. Masa, *ACS Appl. Energy Mater.*, 2020, **3**, 2304–2309.
- 120 T. Zhou, C. Wang, Y. Shi, Y. Liang, Y. Yu and B. Zhang, *J. Mater. Chem. A*, 2020, **8**, 1631–1635.
- 121 S. Ma, Q. Fu, J. Han, T. Yao, X. Wang, Z. Zhang, P. Xu and B. Song, *Adv. Funct. Mater.*, 2024, **34**, 2316544.
- 122 T. Wu, X. Ren, Y. Sun, S. Sun, G. Xian, G. G. Scherer, A. C. Fisher, D. Mandler, J. W. Ager, A. Grimaud, J. Wang, C. Shen, H. Yang, J. Gracia, H.-J. Gao and Z. J. Xu, *Nat. Commun.*, 2021, **12**, 3634.
- 123 A. E. Berkowitz, J. A. Lahut, I. S. Jacobs, L. M. Levinson and D. W. Forester, *Phys. Rev. Lett.*, 1975, **34**, 594–597.
- 124 X. Lyu, Y. Zhang, Z. Du, H. Chen, S. Li, A. I. Rykov, C. Cheng, W. Zhang, L. Chang, W. Kai, J. Wang, L. Zhang, Q. Wang, C. Huang and E. Kan, *Small*, 2022, **18**, 2204143.
- 125 S. Luo, K. Elouarzaki and Z. J. Xu, *Angew. Chem., Int. Ed.*, 2022, **61**, e202203564.
- 126 G. Liu, P. Li, G. Zhao, X. Wang, J. Kong, H. Liu, H. Zhang, K. Chang, X. Meng and T. Kako, *J. Am. Chem. Soc.*, 2016, **138**, 9128–9136.
- 127 X. Han, Y. Yu, Y. Huang, D. Liu and B. Zhang, *ACS Catal.*, 2017, **7**, 6464–6470.
- 128 C. F. Li, J. W. Zhao, L. J. Xie, J. Q. Wu, Q. Ren, Y. Wang and G. R. Li, *Angew. Chem., Int. Ed.*, 2021, **60**, 18129–18137.
- 129 X. Liu, K. Ni, B. Wen, R. Guo, C. Niu, J. Meng, Q. Li, P. Wu, Y. Zhu, X. Wu and L. Mai, *ACS Energy Lett.*, 2019, **4**, 2585–2592.
- 130 H. Yang, G. Vijaykumar, Z. Chen, J. N. Hausmann, I. Mondal, S. Ghosh, V. C. J. Nicolaus, K. Laun, I. Zebger, M. Driess and P. W. Menezes, *Adv. Funct. Mater.*, 2023, **33**, 2303702.
- 131 Y. K. Zhang, C. Q. Wu, H. L. Jiang, Y. X. Lin, H. J. Liu, Q. He, S. M. Chen, T. Duan and L. Song, *Adv. Mater.*, 2018, **30**, 1707522.
- 132 Y. Y. Wu, Y. P. Liu, G.-D. Li, X. Zou, X. R. Lian, D. J. Wang, L. Sun, T. Asefa and X. X. Zou, *Nano Energy*, 2017, **35**, 161–170.
- 133 L. An, J. Li, Y. Sun, J. Zhu, J. Z. Y. Seow, H. Zhang, N. Zhang, P. Xi, Z. J. Xu and C.-H. Yan, *Nano-Micro Lett.*, 2025, **17**, 70.
- 134 B. Kirubasankar, Y. S. Won, S. H. Choi, J. W. Kim, L. A. Adofo, S. M. Kim and K. K. Kim, *Chem. Commun.*, 2023, **59**, 9247–9250.
- 135 Q. Su, Q. Liu, P. Wang, J. Ding, W. Cheng and Y. Huang, *Chem. Eng. J.*, 2024, **483**, 149383.
- 136 N. Zhang, X. Feng, D. Rao, X. Deng, L. Cai, B. Qiu, R. Long, Y. Xiong, Y. Lu and Y. Chai, *Nat. Commun.*, 2020, **11**, 4066.
- 137 T. Wu, S. Sun, J. Song, S. Xi, Y. Du, B. Chen, W. A. Sasangka, H. Liao, C. L. Gan, G. G. Scherer, L. Zeng, H. Wang, H. Li, A. Grimaud and Z. J. Xu, *Nat. Catal.*, 2019, **2**, 763–772.
- 138 Y. Duan, S. Sun, Y. Sun, S. Xi, X. Chi, Q. Zhang, X. Ren, J. Wang, S. J. H. Ong, Y. Du, L. Gu, A. Grimaud and Z. J. Xu, *Adv. Mater.*, 2019, **31**, 1807898.
- 139 C. Liu, D. Ji, H. Shi, Z. Wu, H. Huang, Z. Kang and Z. Chen, *J. Mater. Chem. A*, 2022, **10**, 1336–1342.
- 140 T. Hou, R. Yang, J. Xu, X. He, H. Yang, P. W. Menezes and Z. Chen, *Nanoscale*, 2024, **16**, 15629–15639.
- 141 P. P. Lopes, D. Y. Chung, X. Rui, H. Zheng, H. He, P. Farinazzo Bergamo Dias Martins, D. Strmcnik, V. R. Stamenkovic, P. Zapol, J. F. Mitchell, R. F. Klie and N. M. Markovic, *J. Am. Chem. Soc.*, 2021, **143**, 2741–2750.
- 142 X. Wang, Z. Hou, N. Zhan, Z. Guo and Y. Zhao, *Appl. Catal., B*, 2024, **340**, 123186.
- 143 J. Zhang, Y. Ye, B. Wei, F. Hu, L. Sui, H. Xiao, L. Gui, J. Sun, B. He and L. Zhao, *Appl. Catal., B*, 2023, **330**, 122661.
- 144 D. Xu, S. Liu, M. Zhang, L. Xu, H. Gao and J. Yao, *Small*, 2023, **19**, 2300201.
- 145 Q. Xu, H. Jiang, X. Duan, Z. Jiang, Y. Hu, S. W. Boettcher, W. Zhang, S. Guo and C. Li, *Nano Lett.*, 2021, **21**, 492–499.
- 146 Y. Zhu, Q. Lin, Z. Wang, D. Qi, Y. Yin, Y. Liu, X. Zhang, Z. Shao and H. Wang, *J. Energy Chem.*, 2021, **52**, 115–120.
- 147 J. Wang, S.-J. Kim, J. Liu, Y. Gao, S. Choi, J. Han, H. Shin, S. Jo, J. Kim, F. Ciucci, H. Kim, Q. Li, W. Yang, X. Long, S. Yang, S.-P. Cho, K. H. Chae, M. G. Kim, H. Kim and J. Lim, *Nat. Catal.*, 2021, **4**, 212–222.
- 148 W. Shen, J. Jin, Y. Hu, Y. Hou, J. Yin, Z. Ma, Y.-Q. Zhao and P. Xi, *Chin. J. Catal.*, 2022, **43**, 1485–1492.
- 149 Y. Huang, L.-W. Jiang, B.-Y. Shi, K. M. Ryan and J.-J. Wang, *Adv. Sci.*, 2021, **8**, 2101775.
- 150 Q. Hu, B. Zhu, G. Li, X. Liu, H. Yang, C. D. Sewell, Q. Zhang, J. Liu, C. He and Z. Lin, *Nano Energy*, 2019, **66**, 104194.
- 151 H. Lei, L. Ma, Q. Wan, S. Tan, B. Yang, Z. Wang, W. Mai and H. J. Fan, *Adv. Energy Mater.*, 2022, **12**, 2202522.
- 152 Q. Su, P. Wang, Q. Liu, R. Sheng, W. Cheng, J. Ding, Y. Lei and Y. Huang, *Appl. Catal., B*, 2024, **351**, 123994.
- 153 X. Chen, Q. Wang, Y. Cheng, H. Xing, J. Li, X. Zhu, L. Ma, Y. Li and D. Liu, *Adv. Funct. Mater.*, 2022, **32**, 2112674.
- 154 Y. Zhang, C. Zhang, Y. Guo, D. Liu, Y. Yu and B. Zhang, *J. Mater. Chem. A*, 2019, **7**, 2536–2540.
- 155 L. Gao, X. Cui, Z. Wang, C. D. Sewell, Z. Li, S. Liang, M. Zhang, J. Li, Y. Hu and Z. Lin, *Proc. Natl. Acad. Sci. U. S. A.*, 2021, **118**, e2023421118.

- 156 Q. He, Y. Wan, H. Jiang, Z. Pan, C. Wu, M. Wang, X. Wu, B. Ye, P. M. Ajayan and L. Song, *ACS Energy Lett.*, 2018, **3**, 1373–1380.
- 157 R. Zhang, L. Pan, B. Guo, Z.-F. Huang, Z. Chen, L. Wang, X. Zhang, Z. Guo, W. Xu, K. P. Loh and J.-J. Zou, *J. Am. Chem. Soc.*, 2023, **145**, 2271–2281.
- 158 Y. Li, Z. Zhang, C. Li, X. Hou, J. Zeng, X.-B. Chen, Z. Shi and S. Feng, *Adv. Funct. Mater.*, 2024, 2417983, DOI: [10.1002/adfm.202417983](https://doi.org/10.1002/adfm.202417983).
- 159 H. Chu, R. Li, P. Feng, D. Wang, C. Li, Y. Yu and M. Yang, *ACS Catal.*, 2024, **14**, 1553–1566.
- 160 Z.-Y. Yu, Y. Duan, J.-D. Liu, Y. Chen, X.-K. Liu, W. Liu, T. Ma, Y. Li, X.-S. Zheng, T. Yao, M.-R. Gao, J.-F. Zhu, B.-J. Ye and S.-H. Yu, *Nat. Commun.*, 2019, **10**, 2799.
- 161 Y. Chen, J. Xu, Y. Chen, L. Wang, S. Jiang, Z.-H. Xie, T. Zhang, P. Munroe and S. Peng, *Angew. Chem., Int. Ed.*, 2024, **63**, e202405372.
- 162 L. Zhang, J. Wang, K. Jiang, Z. Xiao, Y. Gao, S. Lin and B. Chen, *Angew. Chem., Int. Ed.*, 2022, **61**, e202214794.
- 163 W. Wan, S. Wei, J. Li, C. A. Triana, Y. Zhou and G. R. Patzke, *J. Mater. Chem. A*, 2019, **7**, 15145–15155.
- 164 Y. Yi, Q. Wu, J. Li, W. Yao and C. Cui, *ACS Appl. Mater. Interfaces*, 2021, **13**, 17439–17449.